International Journal of Heat and Mass Transfer 183 (2022) 122241

Contents lists available at ScienceDirect

International Journal of Heat and Mass Transfer

journal homepage: www.elsevier.com/locate/hmt

Experimental results and interfacial lift-off model predictions of critical heat flux for flow boiling with subcooled inlet conditions – In preparation for experiments onboard the International Space Station

Steven J. Darges[a], V.S. Devahdhanush[a], Issam Mudawar[a,*], Henry K. Nahra[b], R. Balasubramaniam[b,c], Mohammad M. Hasan[b], Jeffrey R. Mackey[d]

[a] Purdue University Boiling and Two-Phase Flow Laboratory (PU-BTPFL), School of Mechanical Engineering, Purdue University, 585 Purdue Mall, West Lafayette, IN 47907, USA
[b] NASA Glenn Research Center, 21000 Brookpark Road, Cleveland, OH 44135, USA
[c] Case Western Reserve University, 10900 Euclid Ave., Cleveland, OH 44106, USA
[d] HX5, LLC, 3000 Aerospace Parkway, Brook Park, OH 44142, USA

ARTICLE INFO

Article history:
Received 16 September 2021
Revised 1 November 2021
Accepted 9 November 2021
Available online 28 November 2021

Keywords:
Flow boiling
Critical heat flux
Subcooled inlet
Flow visualization
Interfacial lift-off model

ABSTRACT

This study investigates critical heat flux (CHF) for subcooled flow boiling of n-Perfluorohexane based on results of pre-launch Earth-gravity Mission Sequence Tests (MSTs) of the Flow Boiling and Condensation Experiment (FBCE), which was launched to the International Space Station (ISS) in August 2021. CHF measurements were made in a rectangular channel having a 2.5 mm by 5 mm cross-section and a 114.6-mm long heated segment. Both single-sided and double-sided heating were tested in vertical upflow in Earth gravity for a variety of inlet conditions. The inlet subcooling was varied in the range of 0.4 – 32.0°C and encompassed both near-saturated and highly subcooled conditions. Experimental trends and high-speed video records were investigated to better understand the mechanism of CHF. Overall trends show CHF increases as flow rate and/or inlet subcooling are increased. Flow features from the events around CHF justify the applicability of the Interfacial Lift-off Model and the determination of limiting criteria for its application. The present experimental data are combined with prior databases for various flow orientations with respect to Earth gravity and microgravity data collected on parabolic flights. Predictions are made using the Interfacial Lift-off Model for this consolidated subcooled-inlet FBCE-CHF database. A heat utility ratio was included in the model to capture the effects of subcooling and corresponding thermodynamic non-equilibrium. An overall mean absolute error of 19.04% indicates good predictive capability of the model for both heating configurations, different gravity environments, and a wide range of inlet subcooling.

1. Introduction

1.1. Two-phase systems in future space missions

Future space missions will dwarf those of the past and present with respect to scope, size, complexity, and duration. Accompanying new, expansive missions will be unique technological challenges such as the need to reduce size and weight of thermal management systems while improving performance. Heat dissipation is commonly handled by single-phase cooling systems which rely solely on a fluid's sensible heat. In contrast, two-phase thermal management systems offer the advantage of utilizing the working fluid's both sensible and latent heat. This results in massive improvements to heat transfer coefficients when compared to traditional single-phase systems. The increased heat transfer effectiveness allows the smaller, lighter, two-phase systems to accomplish the same amount of heat removal as their bulkier single-phase counterparts. Two-phase systems have the potential to play a major role in reducing the size of future onboard thermal control systems (TCSs), which maintain the environment inside a space vehicle, and Rankine power cycles coupled with fission power systems, which demand very high power to mass ratios and look to be integral in future space missions [1,2]. Implementing two-phase thermal management in these applications would involve numerous boiling and condensation processes.

* Corresponding author. https://engineering.purdue.edu/BTPFL.
E-mail address: mudawar@ecn.purdue.edu (I. Mudawar).

https://doi.org/10.1016/j.ijheatmasstransfer.2021.122241
0017-9310/

Nomenclature

A	channel cross-sectional area; area
b	ratio of wetting front length to wavelength
C_1, C_2, C_3	constants
c	wave speed
c_p	specific heat at constant pressure
D	hydraulic diameter
f	friction factor
G	mass velocity, $\dot{m}/A$
g	gravitational acceleration
g_e	gravitational acceleration on Earth
H	height of channel
h	enthalpy
h_{fg}	latent heat of vaporization
Δh_{sub}	h_f - h_b
k	wave number; thermal conductivity
L	length
$\dot{m}$	mass flow rate
N	number of data points
P	perimeter
p	pressure
q''	heat flux
q''_{CHF}	critical heat flux
Re	Reynolds number
T	temperature
ΔT_{sub}	fluid subcooling, $T_{sat} - T_f$
t	time
u	mean phase velocity; velocity
W	width of channel
x	flow quality
x_e	thermodynamic equilibrium quality
y	coordinate normal to interface
z	axial coordinate along flow direction
z_o	axial location where vapor velocity just exceeds liquid velocity
z^*	axial location for determining vapor layer thickness and critical wavelength

Greek symbols

α	void fraction
Γ_{fg}	evaporation rate per unit axial distance
δ	mean vapor layer thickness
ε	heat utility ratio
η	interfacial perturbation
θ	orientation angle of channel
λ	wavelength
μ	dynamic viscosity
ρ	density
ρ''	modified density
σ	surface tension
τ	shear stress

Subscripts

a	corresponding to either heated wall (= 1 or 2)
b	local bulk liquid
c	critical
d	development
e	exit
exp	experimental
f	saturated liquid; bulk fluid
g	saturated vapor
h	heated
i	interfacial
in	inlet
k	either liquid (f) or vapor (g)
n	normal to heated wall
out	outlet
$pred$	predicted
s	solid
sat	saturation
sub	subcooling
tc	substrate thermocouple
w	wall
wa	heated wall (= $w1$ or $w2$)
z	local

Acronyms

BHM	Bulk Heater Module
CHF	Critical Heat Flux
FBCE	Flow Boiling and Condensation Experiment
FBM	Flow Boiling Module
ISS	International Space Station
MAE	Mean Absolute Error (%)
MST	Mission Sequence Testing

The Purdue University Boiling and Two-Phase Flow Laboratory (PU-BTPFL) has spent decades investigating a variety of boiling schemes. They include capillary flow [3], pool boiling [4], falling film [5], macro-channel flow boiling [6], micro-channel flow boiling [7–9], spray cooling [10], jet impingement cooling [11,12], and hybrid of combinations of the other configurations [13]. Each scheme offers performance merits, but also suffers certain shortcomings. However, implementing a two-phase thermal management system in a space vehicle comes with unique design constraints. The ability to operate reliably in a closed loop in microgravity renders both jets and sprays unfavorable. Jets, for example, demand very high flow rates and pose the possibility for surface damage due to impact and erosion. And, with sprays, it is difficult to manage separation of liquid and vapor following impact. Pool boiling is ineffective in microgravity environments due to its reliance on body force to remove vapor from the heated wall and is therefore prone to very low critical heat flux (CHF) values, q''_{CHF}, in microgravity as vapor coalescences unabated along the heated wall [14]. On the other hand, flow boiling remains a viable configuration for thermal management in microgravity. Unlike the aforementioned schemes, flow boiling relies on flow inertia to flush vapor away from the heated wall while operating in a fully closed loop and requires relatively low pumping power.

A plethora of information exists regarding flow boiling and its performance in terrestrial gravity. However, more information is required to optimally implement flow boiling systems in microgravity, where the effect of body force is greatly diminished, and flow behavior will differ from that in Earth gravity. This may impact the accuracy and applicability of many existing databases, correlations, and models that were produced in a terrestrial environment. In order to be confident of system performance in space, it is a necessity to obtain flow boiling data in a reduced gravity environment to better understand the effects of gravity on heat transfer and flow physics.

1.2. Subcooled flow boiling

Heat transfer characteristics of a boiling flow are strongly dependent on the operating conditions of the system. One parameter that can greatly influence the mechanisms of heat transfer is inlet quality. In a flow boiling system, the fluid enters either as a subcooled single-phase liquid (be it highly subcooled or near-saturated) or a two-phase saturated mixture. A fluid that enters in

either a saturated or near-saturated state will predominantly handle heat dissipation by liquid vaporization. Here, the exact mechanism will change as quality increases along the streamwise direction. In lower quality regions, heat dissipation will be in the form of bubble nucleation at the heated wall. As the vapor quality increases, the flow regime transitions from bubbly to slug or churn and eventually annular. At this point, the dominant mechanism of heat transfer becomes evaporation at the liquid-vapor interface.

Highly subcooled inlet conditions involve a more complicated heat transfer process as a portion of the channel will be occupied by the subcooled boiling regime. In this regime, heat dissipation occurs as a combination of single-phase forced convection and bubble nucleation [15–17]. It is also common for vapor bubbles to condense back to liquid as they drift into the subcooled core of bulk liquid. The exact portion of heat transfer each component is responsible for will vary as the bulk temperature of the flow is increased. Up until the onset of nucleate boiling (ONB), only liquid will be present in the channel and heat transfer is entirely facilitated by single-phase forced convection. The subcooled flow boiling region itself can be demarcated based on the physics within the channel [18–20]. Downstream of ONB, the partially developed boiling (PDB) region is entered, where more nucleation sites become active, and the influence of single-phase forced convection decreases. In PDB, the bubbles remain attached to the wall and might slide along it. Bubbles are constrained from getting much larger due to the large condensing effect of the subcooled bulk liquid. As the liquid's subcooling decreases, the point of net vapor generation (NVG) [21] is reached, and bubbles are capable of detaching from the wall and entering the core. This point typically reflects the achievement of fully developed boiling (FDB), where the influence of single-phase convection is negligible. The departed bubbles keep shrinking as they enter deeper into the subcooled liquid and condense. The flow will remain subcooled until the bulk liquid is able to reach saturation temperature.

1.3. Critical heat flux

Perhaps the most important design parameter when it comes to heat-flux-controlled two-phase thermal management systems is CHF [22], which acts as the upper limit to the nucleate boiling regime. During nucleate boiling, liquid along the heated wall is vaporized causing the formation, growth, and departure of vapor bubbles. As bubbles move away from the wall, they are rapidly replaced by the bulk liquid in a cyclical manner. This process yields high heat transfer coefficients and relatively low surface temperatures making it the ideal operating range for efficient heat dissipation. Nucleate boiling is sustained up until CHF, which occurs when the bulk liquid is no longer able to access the heated wall and bubble nucleation at the wall comes to a halt. The heat dissipation mechanism then shifts to film boiling, in which, a layer of vapor occupies the region adjacent to the heated wall. Heat is transferred through the vapor to the interface where evaporation occurs, however, due to the low thermal conductivity of vapor, wall temperatures are drastically higher than those in the nucleate boiling regime. The transition from the nucleate to film boiling regime is abrupt and manifests as a rapid unsteady rise in surface temperature as heat transfer coefficients plummet. This leads to overheating, burn out, and system failures.

Due to the catastrophic nature of CHF, the development of design tools to predict CHF is of the utmost importance. Researchers have aimed to accomplish this through two main avenues. First are readily available empirical correlations based off experimental data. Correlations have their limitations, and their application is not always appropriate. Many correlations are developed for a limited range of fluids, operating conditions, and geometries. Because of this, extrapolation of correlations to previously untested operating conditions can be unpredictable and result in wild inaccuracies [22,23].

The other avenue used for CHF prediction is analytical models. These are derived from the underlying mechanisms of CHF and are coupled with empirical constants to obtain closure. Analytical models generally have broader applications than most correlations, however, they are scarcely available in the literature. Some available models are *Boundary Layer Separation, Bubble Crowding, Sublayer Dryout*, and *Interfacial Lift-off*. The *Boundary Layer Separation Model* developed by Kutateladze and Leont'ev [24] utilizes an analogy between vapor effusion from the heated wall and gas injection into a liquid boundary layer. As the gas velocity is increased to a critical value, the velocity gradient near the wall will decrease and, the boundary layer separates from the wall. This is compared to vapor effusion during flow boiling reaching a production rate that prevents liquid replenishment at the wall triggering CHF. The *Bubble Crowding Model* developed by Weisman and Pei [25] postulates that CHF occurs when vapor production results in a dense bubbly layer adjacent to the heated wall that suppresses turbulent fluctuations of liquid from accessing the heated wall. The *Sublayer Dryout Model* proposed by Lee and Mudawar [26] considers a vapor blanket that forms near the wall and traps a sublayer of liquid near the wall. This sublayer is replenished from the bulk liquid and CHF occurs when the heat dissipation requirements exceed the potential of the replenished liquid to dissipate the heat. The *Interfacial Lift-off Model* postulated by Galloway and Mudawar [27,28], based on extensive visual observation, describes a wavy vapor layer along the heated wall. The troughs of the interfacial waves, termed wetting fronts, allow liquid access to the heated wall where intense boiling occurs as it propagates down the heated wall. CHF is postulated to occur when vapor momentum at the wetting fronts causes it to lift off the wall and boiling is impeded.

Zhang *et al.* [29] attempted to encapsulate the effect subcooling will have on CHF by the development of a heat utility ratio. The heat utility ratio is meant to describe the partitioning of heat transferred to the fluid in forms of sensible and latent heat. The developed correlation is based on experimental CHF results from their own study as well as Sturgis and Mudawar [30,31]. Through the incorporation of the heat utility ratio, Zhang *et al.* [29] and Kharangate *et al.* [32] were able to achieve success in predicting the effects of subcooling.

1.4. Objectives of present study

The present study is part of PU-BTPFL and NASA Glenn Research Center's collaborative Flow Boiling and Condensation Experiment (FBCE), that will collect invaluable flow boiling and condensation data in microgravity on the International Space Station (ISS). This study aims to investigate CHF for subcooled flow boiling of nPFH in Earth gravity. The results of the pre-launch Earth-gravity experiments (called Mission Sequence Testing; MST) of FBCE's Flow Boiling Module (FBM), which was launched to the ISS in August 2021, are presented. The flow configuration is vertical upflow boiling with both single-sided and double-sided heating; reasons for choosing these configurations are given in detail in [33]. Essentially, (i) vertical upflow yields the highest q''_{CHF} in Earth gravity and is most similar to microgravity with respect to flow symmetry within the channel and (ii) single- and double-sided heating were experimented to enable simultaneous visualization of flow boiling while heating and to observe the evolution of vapor layer with and without any interaction from other walls (note that heating more than two walls would induce more three-dimensionality to the flow and diminish the quality of visualization. The interfacial lift-off model is adopted to make predictions for a consolidated subcooled-inlet FBCE-CHF database of this MST data and some older FBCE databases [32,34].

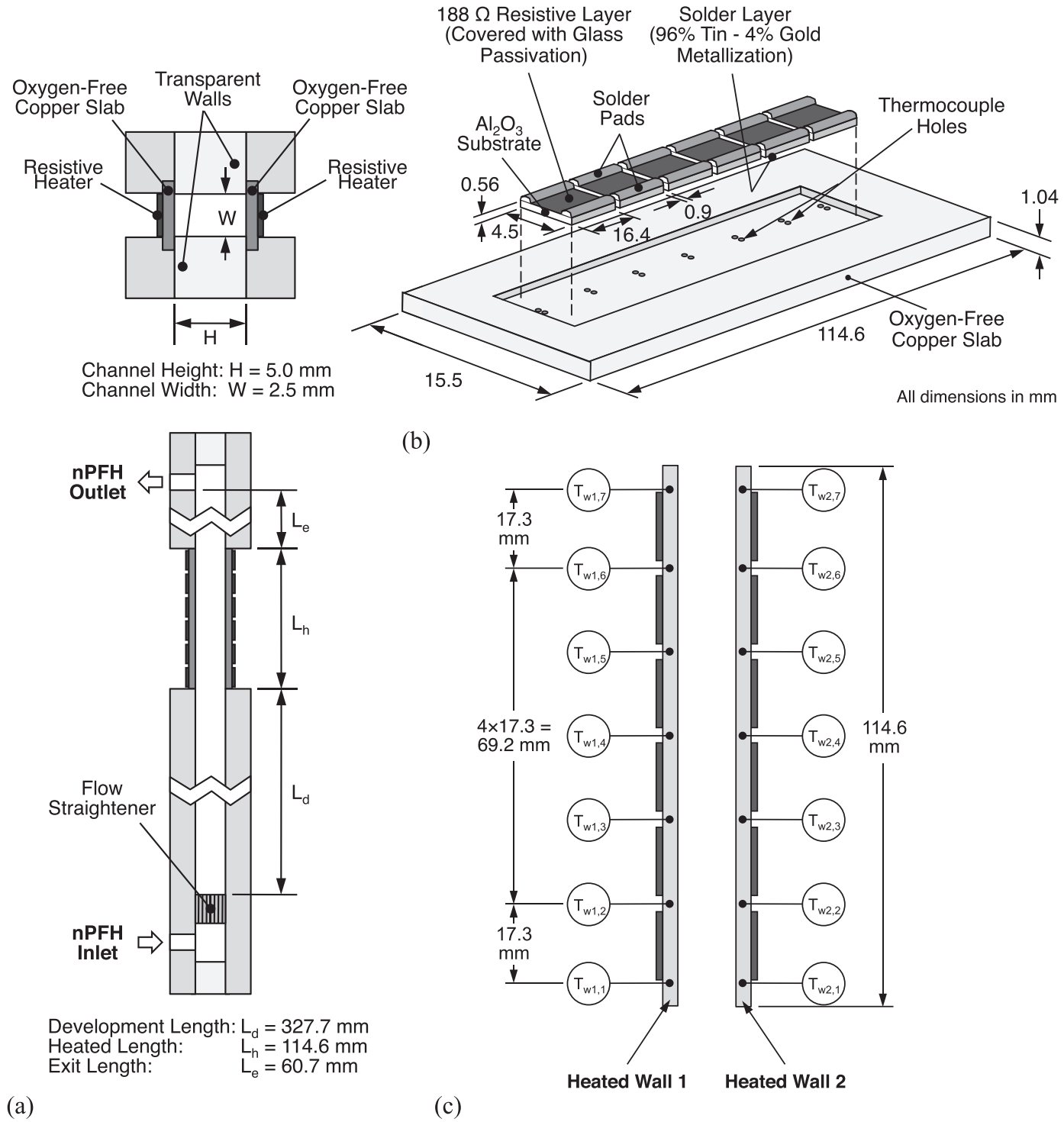

Fig. 1. Schematic representations of (a) overall construction of Flow Boiling Module (FBM), (b) construction of heating slabs, and (c) substrate temperature measurement.

2. Experimental methods

2.1. Flow boiling module

A schematic diagram of the overall construction of the Flow Boiling Module (FBM) is shown in Fig. 1(a). The FBM is mainly comprised of three transparent polycarbonate plates sandwiched together between two aluminum support plates. The support plates offer structural integrity to the FBM, helping prevent buckling and evenly spreading out bolting stresses. The flow channel is formed by milling a 5.0-mm deep and 2.5-mm wide rectangular slot into the middle polycarbonate plate. The flow channel is made up of three sections: an upstream 327.7-mm development length, a middle 114.6-mm heated length, and a downstream 60.7-mm exit length. The development length serves to allow the flow to become hydrodynamically fully developed before it enters the heated section. The heated length is made by inserting two oxygen-free copper heating slabs into the middle plate on opposite sides of the flow channel. The other two channel walls within the heated length are made of polycarbonate for flow visualization and as-

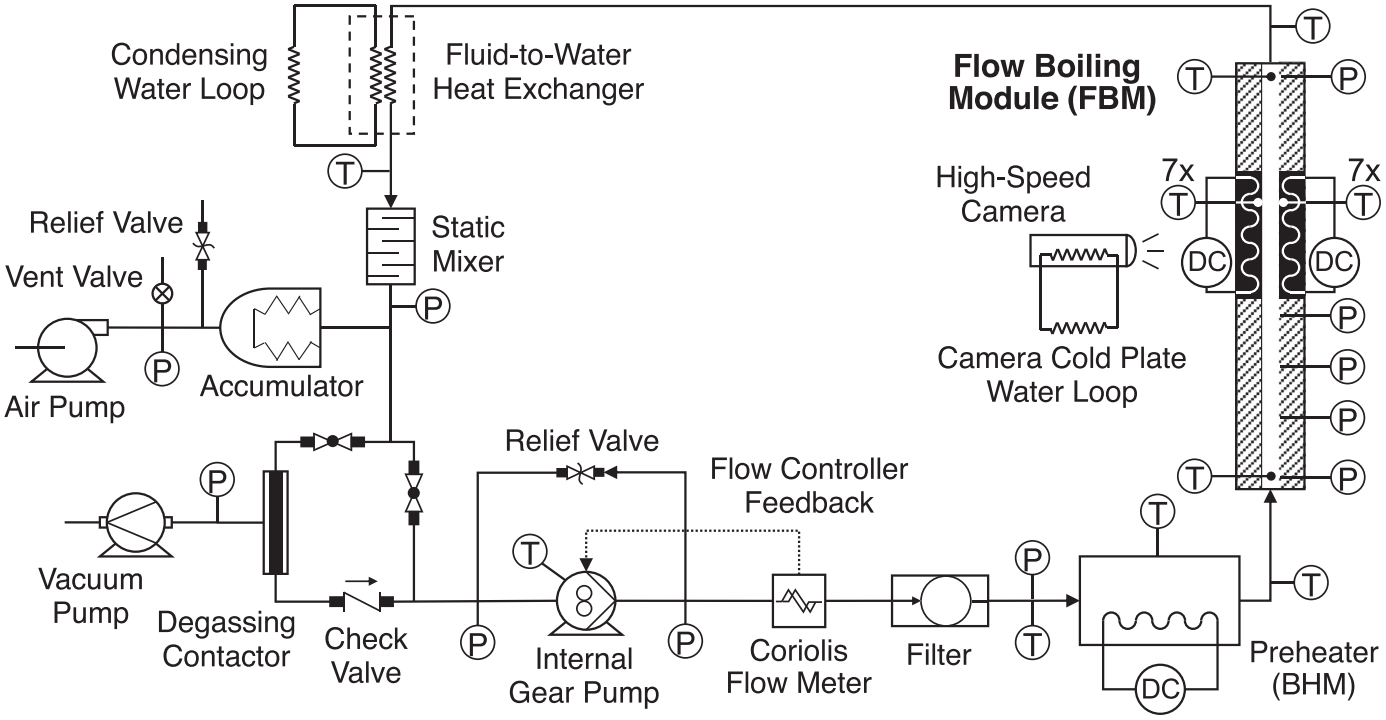

Fig. 2. Schematic diagram of experimental two-phase flow loop.

sumed to be adiabatic during data analysis. Each heating slab is of dimensions 114.6-mm length, 15.5-mm width, and 1.04-mm thickness, and one side of each slab is in contact with the fluid and forms the heating surface. As shown in Fig. 1(b), on the other side of each slab are affixed a set of six thick-film resistive heaters of dimensions 16.4-mm length, 4.5-mm width, and 0.56-mm thickness in series. This is done by soldering with a 96% tin and 4% gold composition. Each successive heater is separated by 0.9 mm to allow for the placement of substrate thermocouples. The heaters are themselves made of an aluminum oxide substrate with a 188-Ω resistive layer on its underside stretched between two solder pads. Uniform heat flux distribution across the heating surface is ensured by using heaters with the exact identical electrical resistance and wiring them in parallel to a DC power supply. This heated wall design allows for fast temperature response and accurate CHF measurement [35,36]. A maximum of 175 W power can be supplied to each heating slab.

The fluid entry and exit ports of the FBM are placed at 90° angles to the flow channel, but any large eddies are broken up and flow streamlines straightened out by affixing a honeycomb core close to the inlet. All solid-solid interfaces within the FBM are made leak-proof by using NBR, HNBR, and neoprene O-rings.

2.2. Flow loop

Fig. 2 shows a schematic of the two-phase flow loop used to supply the working fluid, normal-Perfluorohexane (nPFH), at conditions desired at the FBM inlet. A magnetically-coupled internal gear pump positively displaces the fluid in pure liquid state. A bypass relief valve is provided across the ends of the pump and set to crack open if the pressure at the pump exit is higher than that at the pump inlet by more than 29.00 psid (199.95 kPa). Another relief valve is provided in parallel as a backup and cracks open at 30.00 psid (206.84 kPa). The liquid then passes through a Coriolis flow meter, where its flow rate is measured, and feedback is given to the pump so that its speed of rotation can be adjusted to deliver the desired flow rate. After passing through a filter, where any possible impurities in the fluid are removed, the flow enters the preheater (also called the Bulk Heater Module; BHM), where a substantial amount of heat is added to the fluid to adjust the fluid's temperature and void fraction (in some cases), and thereby the FBM inlet quality. The preheater is equipped with a set of DC-powered heaters and instrumented with both thermocouples and Resistance Temperature Detectors (RTDs) that shuts down all heaters in case the heating surface exceeds 130°C or the downstream fluid 100°C for safety. The fluid enters the FBM as either a subcooled liquid or saturated two-phase mixture, gains heat, and exits the FBM as either a subcooled liquid or two-phase mixture. All heat gained by the fluid is lost in a fluid-to-water stainless-steel tube-in-tube heat exchanger (with a spiral finned inner tube) to a condensing water loop and exits in a subcooled state. This fluid is thoroughly mixed in a static mixer to ensure thermodynamic uniformity and the condensation of any possible vapor bubbles. The fluid in a highly subcooled pure liquid state re-enters the pump.

An accumulator, which helps maintain a set reference pressure point and avoid two-phase instabilities in the loop [37], is connected to the main flow loop at a T-junction located immediately downstream of the static mixer. Within the stainless-steel accumulator, most of the fluid is stored on one side of stainless-steel bellows, whereas the other side is filled with air, the pressure and volume of which is controlled by an air pump and a vent valve. A relief valve is provided on the air-side for safety purposes and is set to crack open at 20.00 psig (137.90 kPa difference across ends).

A degassing contactor, used to degas the fluid (i.e., remove all non-condensable gasses from the fluid) and enhance the accuracy of collected two-phase data, is provided parallel to the section of the flow loop between the above-mentioned T-junction and the pump. Its main component is a semi-permeable membrane; the fluid flows on one side and vacuum is applied on the other side using a vacuum pump.

Most valves in the flow loop are solenoid actuated to allow for remote operation. The secondary water loops are equipped with their own flow meters, valves, flow controllers, pressure transduc-

ers, and RTDs, all of which are essential to the operation of the entire flow loop, but the details are outside the scope of this study.

2.3. Instrumentation and measurement uncertainty

As shown in Fig. 2, five local pressure measurements are made within the FBM using absolute pressure transducers: one each near the inlet and outlet, and three at intermediary locations within the development length. Fluid temperatures very close to the FBM inlet and outlet are measured using type-E thermocouples sticking into the flow. As shown in Figs. 1(b) and 1(c), seven local substrate temperatures are measured for each heating slab at equidistant locations along the flow direction using two sets of seven type-E thermocouples inserted into shallow holes (resembling hemispherical indentations). One set is used for data collection and software reset at 122°C, usually an aftermath of CHF. The other set is part of the hardware safety circuitry, and it provides feedback to a relay that shuts down both the BHM and FBM heaters in case any temperature exceeds 132°C and the software reset fails. Local pressures and temperatures are measured and monitored at numerous points of the flow loop using pressure transducers and both thermocouples and RTDs, respectively.

To enable conducting both single-sided and double-sided heated wall experiments, DC power can be supplied to either one or both heating slabs independent of each other. Both the current and voltage of DC power input to each set of FBM heaters and the preheater heaters are measured. Flow rate is measured in a Coriolis flow meter of range 0 – 60 g/s.

All temporal sensor output signals are collected and measured using a set of two data acquisition systems (2 DAQs; one for thermocouple data and the other for other sensors). The housekeeping data are recorded at a rate of 1 Hz, and during FBM runs, at an increased rate of 5 Hz. The DAQ and all other instruments (including solenoid valves) are controlled by in-house FBCE flight software.

Maximum uncertainties in the measurements of temperature (using thermocouples), temperature (using RTDs), absolute pressure, FBM heater power, preheater power, and flow rate are ±0.5°C, ±0.5°C, ±0.7 kPa, ±0.3% of reading, ±0.6% of reading, and ±0.6% of reading, respectively. Approaching CHF, the incremental increase in heat flux is less than 2 W/cm^2. As discussed in the following section, the recorded q''_{CHF} is an average between the heat flux resulting in an excursion of wall temperatures and the previous steady step. This yields a CHF isolation error (difference between the true q''_{CHF} and the q''_w which triggered CHF) of ~1 W/cm^2. However, 6 cases exist in which the final step was greater than 2 W/cm^2; the maximum CHF isolation error experienced in these cases is ~4 W/cm^2.

2.4. Flow visualization techniques

FBM's design, especially the transparency of the polycarbonate plates, provides excellent optical access to the boiling flow within the heated section. All three polycarbonate plates were vapor polished to minimize vignetting effects to those produced solely by the opaque copper heaters and O-rings necessary to seal the test module. High-speed photography techniques are used to record the intricate features of two-phase flows and capture events that lead to CHF for each operating condition.

The high-speed camera is equipped with a F#0.95–25 mm focal length lens and captures photographs of resolution 2040 × 164 pixels at a frame rate of 2000 frames/s and a shutter speed of 10 μs. Based on verification test data, the actual spatial resolution achieved by the imaging system is better than 100 µm. The opposite transparent wall is backlit with blue light emitting diodes (LEDs) and a light-shaping diffuser with an intermediate sheet of Teflon required due to the extremely short light transmission distance.

The heat generated by the high-speed camera during operation is removed from a respective cold plate by cooling water fed from an external source (for the future ISS experiments, this would be the ISS cooling water).

2.5. Operating procedure

As already mentioned, the ultimate goal of the present experimental setup is to be installed and tested onboard the ISS, and hence, its operation will have to be done remotely. After installation, the entire test matrix will be completed in space without any in-person intervention, and both sensor-measured data and photography data will be sent to the personnel on Earth. This study, reporting data from the MST (the final set of vertical upflow experiments in Earth gravity), was conducted in the same manner as it will be aboard the ISS.

The fluid is degassed before the start of testing and at regular intervals thereafter as needed. For each boiling curve, the FBM inlet conditions (flow rate, inlet pressure, inlet subcooling, and inlet quality) are set and the flow loop allowed adequate time to reach them. Power is supplied to one or both FBM heating slabs in small increments from zero until CHF is reached. Each increment is for a fixed time period of 120 s, which has been deemed to be sufficient to attain steady-state in prior studies [35,36] of nucleate boiling in FBM. This was later verified from preliminary testing for this study. Although CHF is defined as the heat flux increment which leads to an unsteady rise in surface temperature, for safety and consistency, CHF is designated as the heat flux increment which causes at least one of the slab thermocouples to exceed 122°C. FBM heater power is brought down to a minimum power level by FBCE software as soon as a temperature of 122°C, recorded by any of the data thermocouples, is reached. A hardware shutdown of all heaters is invoked at 132°C as a safety precaution both to prevent any damage to the FBM and to avoid the breakdown of nPFH, which might lead to the formation of the toxic substance perfluoroisobutene (PFiB). Temporal data from all sensors and high-speed images are recorded. The above procedure is repeated for other predetermined FBM inlet conditions.

2.6. Data processing and operating conditions

The latest 20 s of the temporal data of the heat flux increment preceding CHF are averaged to obtain the steady-state operating conditions corresponding to CHF; more details are available in [33]. The measured local substrate temperatures, T_{tc}, are first translated into surface temperatures, T_w, by accounting for the minor copper conductive resistance between the two points. By assuming both a constant heat flux across the heating slab and one-dimensional heat conduction through the thickness, this is done as

$$T_w = T_{tc} - \frac{q''_w H_{tc}}{k_s}, \tag{1}$$

where q''_w is heat flux, H_{tc} conduction height (= 0.483 mm), and k_s pure copper conductivity. These surface temperatures are designated as $T_{wa,z}$, where wa is the heated wall ($w1$ or $w2$) and z the streamwise measurement location (1 upstream through 7 downstream) as shown in Fig. 1(c).

The fluid enthalpy at FBM inlet is determined as

$$h_{in} = h|_{T_{in},\,p_{in}}, \tag{2}$$

where T_{in} and p_{in} are the FBM inlet fluid temperature and pressure, respectively. And the fluid enthalpy at FBM outlet is determined from an energy balance as

$$h_{out} = h_{in} + \frac{q''_w P_h L_h}{\dot{m}}, \tag{3}$$

Table 1
Summary of MST CHF data points with subcooled inlet conditions.

	Single-Sided Heating	Double-Sided Heating
Mass velocity, G	180 – 3200 kg/m^{2}s	180 – 3200 kg/m^{2}s
Mass flowrate, $\dot{m}$	2.25 – 40.00 g/s	2.25 – 40.00 g/s
Inlet pressure, p_{in}	119.9 – 171.1 kPa	125.4 – 190.8 kPa
Inlet temperature, T_{in}	34.3 – 71.6°C	35.8 – 73.0°C
Inlet subcooling, $\Delta T_{sub,in}$	0.4 – 31.6°C	0.9 – 32.0°C
Inlet quality, $x_{e,in}$	−0.420 – −0.003	−0.445 – −0.003
Outlet pressure, p_{out}	113.2 – 167.9 kPa	120.7 – 172.3 kPa
Outlet temperature, T_{out}	39.9 – 71.4°C	45.2 – 72.1°C
Outlet subcooling, $\Delta T_{sub,out}$	0 – 20.5°C	0 – 17.1°C
Outlet quality, $x_{e,out}$	−0.222 – 0.200	−0.198 – 0.457
Critical heat flux, q''_{CHF}	14.2 – 50.6 W/cm^2	14.2 – 43.6 W/cm^2

where $\dot{m}$ is the mass flow rate through the FBM. For the two heating configurations used in this study, the heated perimeters are

$$P_h = \begin{cases} 2W, & \text{double-sided heating} \\ W, & \text{single-sided heating} \end{cases}, \tag{4}$$

where W is the channel width. Thermodynamic equilibrium qualities at the FBM inlet and outlet are determined from the relation

$$x_e = \frac{h - h_f\big|_p}{h_{fg}\big|_p}, \tag{5}$$

where $h = h_{in}$ or h_{out} is the actual fluid enthalpy at the module inlet/outlet, and both h_f, the enthalpy of the saturated liquid, and h_{fg} are based on the measured inlet/outlet pressure.

q''_{CHF} is determined by averaging the heat flux that caused the temperature excursion and the previous steady heat flux. This is done because the true q''_{CHF} will fall somewhere between the previous steady increment and the new unstable one. However, the operating conditions corresponding to CHF are taken from the steady heat flux increment directly before CHF. This is because the operating conditions at the next heat flux that undergoes CHF never reach a steady period that can be used for averaging.

All thermophysical properties of nPFH are obtained from NIST-REFPROP [38]. Important parameter ranges for the CHF data points from MST experiments with subcooled inlet are reported in Table 1 for single- and double-sided heating separately.

3. Experimental CHF results

3.1. Flow visualization results

Throughout data collection, high speed photographic images of the test section's heated length were recorded with the goal to capture events leading up to and initiating CHF. Images are captured for both single-sided and double-sided heating for a variety of operating conditions. The focus of the images presented is the interfacial behavior just prior to CHF (indicated as CHF–), as CHF occurs and excursions of wall temperatures begin (CHF transient), and post CHF occurring as wall temperatures continue to increase (indicated as CHF+). The following results justify the applicability of the *Interfacial Lift-off Model* used to predict CHF in section 4.

3.1.1. Single-sided heating at high mass velocities

Fig. 3 shows sequential images recorded around CHF for single-sided heating with G = 1600 kg/m^{2}s, p_{in} = 130.3 kPa, $\Delta T_{sub,in}$ = 4.6°C, $x_{e,in}$ = −0.062, and a resulting CHF value of q''_{CHF} = 36.74 W/cm^2. The time elapsed between consecutive images in Fig. 3, and all other figures unless noted otherwise, is 1.5 ms (*i.e.*, every third photographed image). As shown in the images corresponding to CHF–, near-saturated liquid enters the channel and vaporizes quickly along the heated wall at the leading edge. The vapor patches slide along the channel wall and grow as boiling ensues. However, in the upstream region, distinct gaps remain between vapor patches. The gaps between vapor patches, or wetting fronts, allow liquid to access the heated wall and boil. During the CHF transient, as boiling persists in the wetting fronts, vapor production eventually prevents liquid access to the heated wall and the wetting front lifts off the wall. Lift-off initiates at the wetting front furthest downstream and causes heat to be conducted to other nearby wetting fronts. This results in a chain reaction as the adjacent upstream wetting front undergoes lift off. At CHF+, it is observed that wetting fronts farther upstream have been extinguished resulting in a continuous wavy vapor layer next to the wall. The process of successive wetting fronts lifting off the heated wall brings boiling to a halt and is determined to be the trigger mechanism that causes CHF.

Fig. 4 shows sequential images recorded around CHF for single-sided heating with G = 3200 kg/m^{2}s, p_{in} = 138.6 kPa, $\Delta T_{sub,in}$ = 7.4°C, $x_{e,in}$ = −0.100, and a resulting q''_{CHF} = 41.73 W/cm^2. Similar physical details are seen between CHF–, CHF transient, and CHF+ as those captured in Fig. 3. At CHF–, wetting fronts are bountifully present in the upstream portion of the channel. As CHF is initiated, seen in CHF transient, wetting fronts are extinguished along the heated wall until CHF+, where a continuous wavy vapor layer occupies much of the heated wall. Compared to the images shown in Fig. 3 with a lower flowrate, the mean thickness of the vapor patches is thinner in Fig. 4. It is also observed that the length of vapor patches, and thus distance between wetting fronts or wavelength of the liquid-vapor interface, decreases when compared to the lower flow rate case in Fig 3. This is particularly noticeable in the upstream region of the channel where the mean vapor layer thickness is relatively small compared to the height of the channel. The increased number of wetting fronts, and decreased wavelength of the interface, promote heat removal from the wall, which results in a higher q''_{CHF} than the case depicted in Fig. 3.

3.1.2. Double-sided heating at high mass velocities

Fig. 5 shows sequential images recorded around CHF for double-sided heating with G = 1600 kg/m^{2}s, p_{in} = 153.3 kPa, $\Delta T_{sub,in}$ = 8.2°C, $x_{e,in}$ = −0.113, and a resulting q''_{CHF} = 37.80 W/cm^2. At CHF–, vapor formation has initiated the formation of a wavy vapor layer along both heated walls, albeit with some asymmetry resulting from one or more of the following reasons, i) minute differences in wall heat applied to the opposite walls, ii) a very slight tilt of the FBM, or iii) microscopic imperfections on one wall causing preferential vapor formation. The patches of vapor and wetting fronts propagate downstream until the vapor layers on each wall grow large enough to merge with one another and interfacial curvature is lost. During CHF transient, one of the walls, in this case the left, experiences CHF as its wetting fronts begin to extinguish. By the end of CHF transient and into CHF+, the entire wall is coated by a wavy vapor layer as all wetting fronts lifted off the wall. However, again due to the minute asymmetry, the opposite heated wall still has some wetting fronts intact upstream and cooling proceeds. The process exhibited in Fig. 5 shows the mechanism of CHF for the double-sided heating configuration, even with a relatively high inlet pressure, agrees with the mechanism shown in Figs. 3 and 4.

3.1.3. Single- and double-sided heating at low mass velocities

Fig. 6(a)–(d) show sequential images during CHF transient for G = 200 kg/m^{2}s and highly subcooled single-sided heating, highly subcooled double-sided heating, near-saturated single-sided heating, and near-saturated double-sided heating, respectively. One notable difference between the images shown for these relatively low

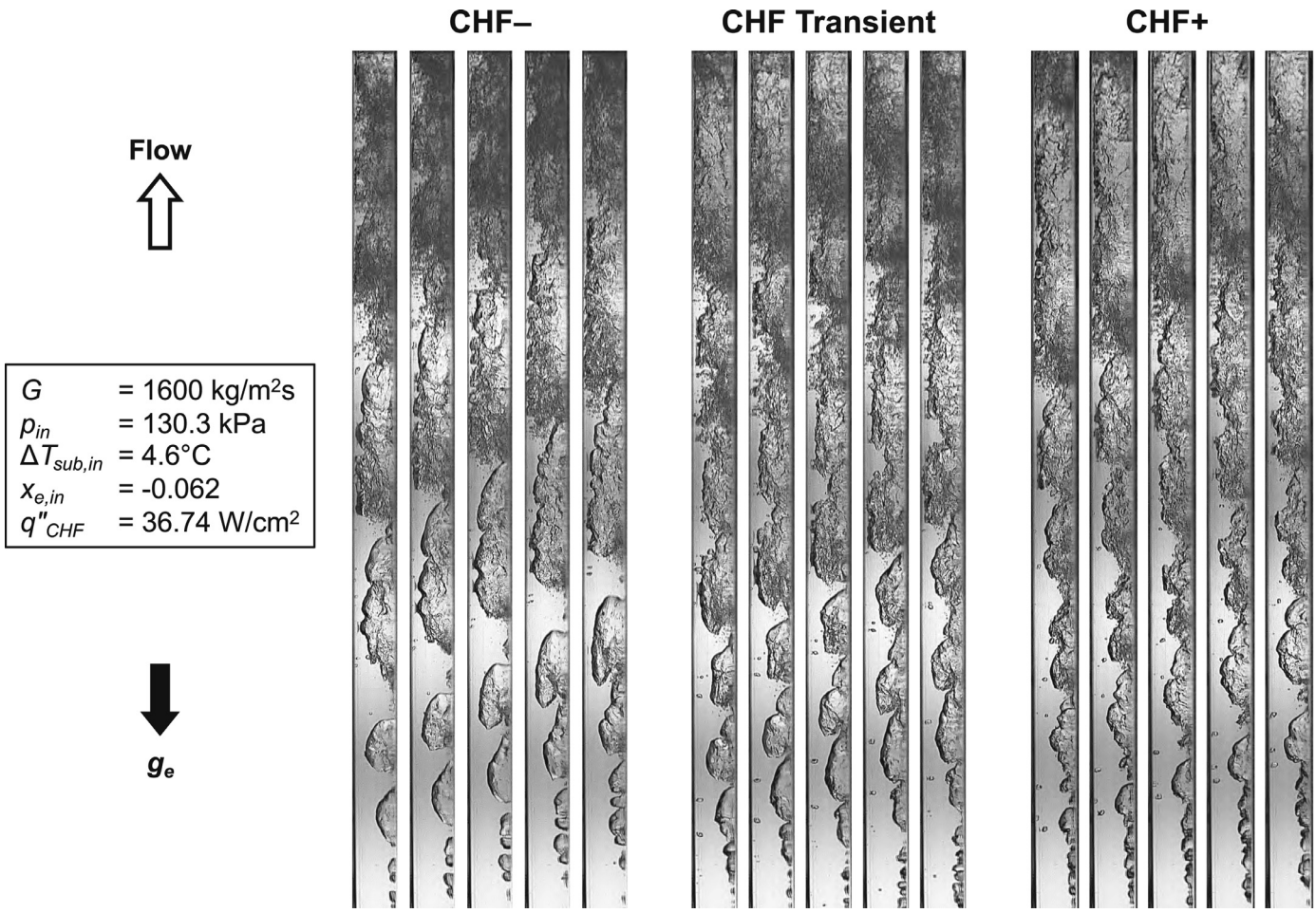

Fig. 3. Sequential images during CHF–, CHF transient, and CHF+ for G = 1600 kg/m^{2}s, p_{in} = 130.3 kPa, $\Delta T_{sub,in}$ = 4.6°C, $x_{e,in}$ = −0.062, and q''_{CHF} = 36.74 W/cm^2 with single-sided heating. The interval between successive images in all sequences is 1.5 ms.

mass velocity cases and the high mass velocity cases in Figs. 3–5 is the impact of weak flow inertia. A distinct difference between the sequences in Fig. 6 and those in the previous figures is absence of a distinct wavy vapor layer that forms near CHF and eventual wetting front lift off for most conditions. These differences are closely related to the relatively weak inertial effects in Fig. 6, which suggests the physical mechanism causing CHF is different from that in Figs. 3–5.

For the highly subcooled single-sided heating case, Fig. 6(a), relatively small patches of vapor are observed moving through the channel along the heated wall. Significant amounts of vapor appear to be condensing into liquid as some of the vapor detaches from the wall. For the double-sided case shown in Fig. 6(b), vapor patches are present along both heated walls. In the upstream region, liquid can access the heated wall in between vapor patches. However, due to the low velocity and increased heat addition from both walls compared to Fig. 6(a), the vapor patches grow to a more considerable size downstream and the vapor layers merge. Compared to previous higher flowrate cases, Figs. 3–5, fluid travels much slower through the channel. As wall temperatures begin to rise and CHF occurs, wetting fronts are still present along both walls, and a continuous vapor layer does not block liquid access to the heated wall as it does in Fig. 5. In this case, the mechanism of CHF is relatively complex due to the vapor from both heated walls merging to form a large vapor entity which occupies the majority of the downstream region. Regardless of the wall temperatures exceeding 122°C and CHF occurring, wetting fronts are still present in the upstream region. Hence, interfacial lift-off is not the mechanism causing CHF for these conditions.

The near-saturated cases again show different flow characteristics than those of higher flow rates or higher subcooling. The near-saturated cases at low mass velocities are dominated by periodic waves of liquid and vapor moving through the channel. Fig. 6(c) shows sequential images, with 200 ms between images, for single-sided heating with a near-saturated inlet; choosing a large time interval for this case is intended to capture important periodic changes in flow structure not encountered at other conditions. In the first image of this sequence, almost all liquid is present in the channel and only a small amount of vapor is present along the left heated wall. As time progresses, large amounts of vapor can be seen in the upstream section of the channel over the next three images. The vapor occupying the upstream region of the test section is a result of non-equilibrium effects occurring within the preheater convecting into the test section. At the same time, smaller waves of vapor can be seen moving quickly though the channel in the downstream section as the large patches upstream break up. In the final image, again mostly liquid is present in the channel as the vapor convects out of the channel. Throughout the entire process, a thin layer of vapor remains along the heated wall. The observed cycle of varying ratios of liquid and vapor present in the channel resembles the density wave oscillations (a type of two-phase flow instability) observed by O'Neill and Mudawar [39] during vertical upflow in the FBM. At certain times, as vapor moves through the channel and coalesces with the thin layer adjacent to

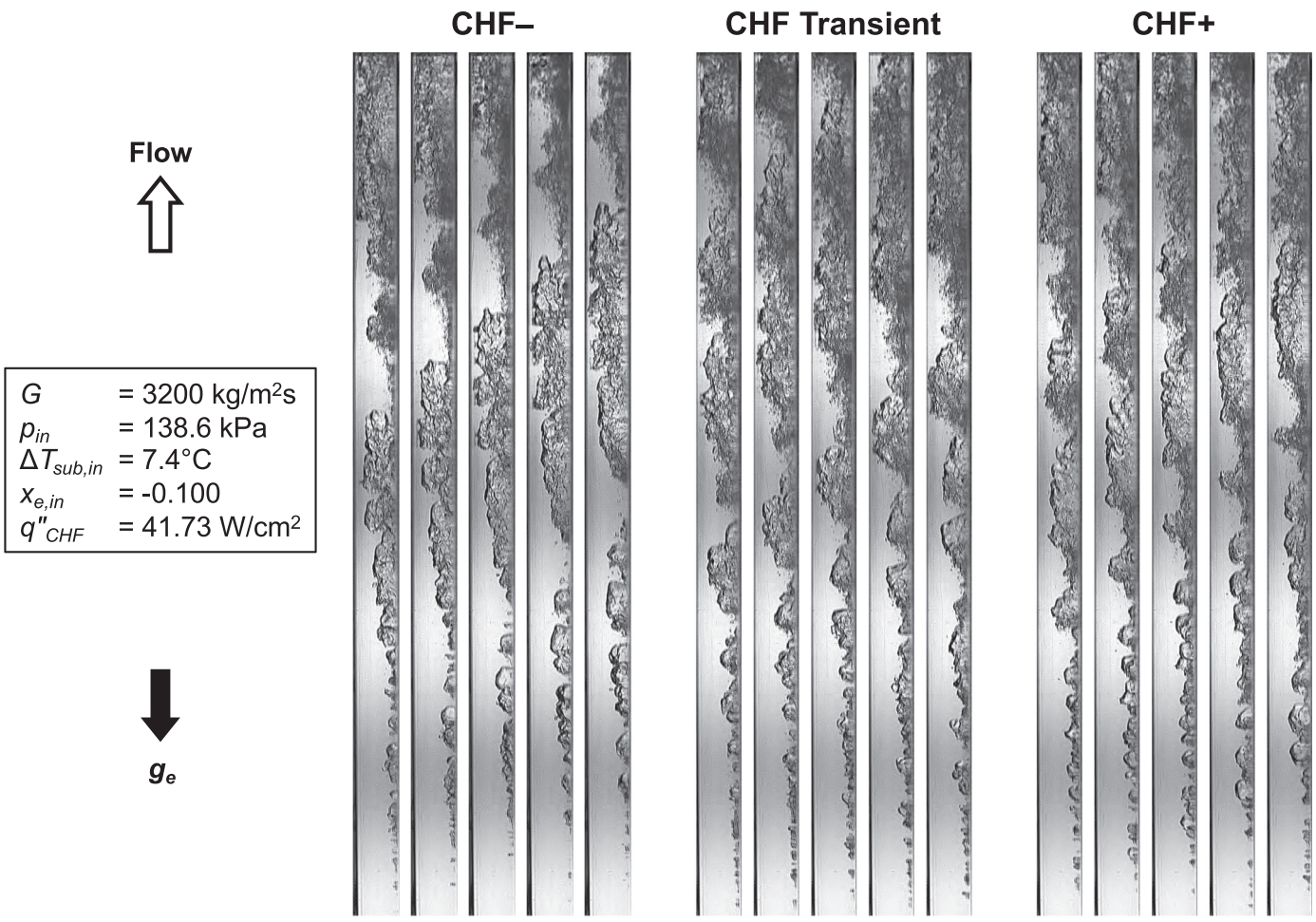

Fig. 4. Sequential images during CHF–, CHF transient, and CHF+ for G = 3200 kg/m^{2}s, p_{in} = 138.6 kPa, $\Delta T_{sub,in}$ = 7.4°C, $x_{e,in}$ = −0.100, and q''_{CHF} = 41.73 W/cm^2 with single-sided heating. The interval between successive images in all sequences is 1.5 ms.

the wall, the vapor layer can be seen to locally thicken. A similar trend is seen in the sequential images, with 37 ms spacing, of double-sided heating shown in Fig. 6(d). The first image depicts predominantly liquid in the channel. This is followed by two images that show large vapor layers upstream on both heated walls, like the wavy vapor layer seen at higher velocities. However, the vapor patches on the wall quickly grow towards the middle of the channel and do not slide along the wall. They are also present periodically and are not maintained long enough for lift-off to occur. Eventually, vapor layers merge and propagate through the channel as they mix. In the fourth image, the majority of vapor has exited the channel and a small amount of vapor is present in the channel. In the final image, almost all the vapor has been removed. For both near-saturated cases, these cycles repeat leading up to CHF.

3.2. CHF trends

Figs. 7(a) and 7(b) show plots of measured q''_{CHF} versus mass velocity for vertical upflow with single-sided and double-sided heating, respectively. For each heating configuration, the inlet conditions are loosely divided into two subcooling ranges: highly subcooled for $\Delta T_{sub,in} > 10$°C and near-saturated for $0 < \Delta T_{sub,in} \leq 10$°C. In either heating configuration, the highly subcooled range exhibits higher q''_{CHF} than the near-saturated for the same mass velocity. This is the outcome of the former featuring the ability to absorb more of the supplied heat in the form of sensible heat, which is reflected by more superior vapor condensation. For the highly subcooled range, most bubbles are condensed into the bulk liquid after detachment or even while attached to the heated wall, allowing better liquid access to and replenishment of the heated wall. Here, some of the wall heat is used up to bring the replenishment bulk liquid to the superheat necessary for bubble nucleation and growth. This behavior is captured in Figs. 6(a) and 6(b), where CHF is associated with formation of rather small and localized insulating vapor patches (rather than a continuous wavy vapor layer). Notice in both Fig. 7(a) and (b) that, for each subcooling range, q''_{CHF} increases monotonically with increasing mass velocity, with the dependence being more pronounced at lower mass velocities. It must be emphasized that higher mass velocity not only increases the amount of sensible and latent heat of the working fluid, but also results in higher inertial and shear forces that hasten vapor removal from the channel. Comparing the results for single-sided heating, Fig. 7(a), to those for double-sided, Fig. 7(b) shows the latter yields lower q''_{CHF} due to vapor structures from both walls interacting with one another, in addition to twice the amount of heat being supplied to the working fluid for the same heat flux. These q''_{CHF} differences between the two heating configurations are large for highly subcooled inlet where the fluid's condensing capability plays an important role on CHF delayal. With the double-sided having weaker condensation due to the fluid's higher temperature and larger vapor void fraction, q''_{CHF} is smaller. These effects are more pronounced at low flow rates, as confirmed by flow visualization; note how the single-sided in Fig. 6(a) has less vapor

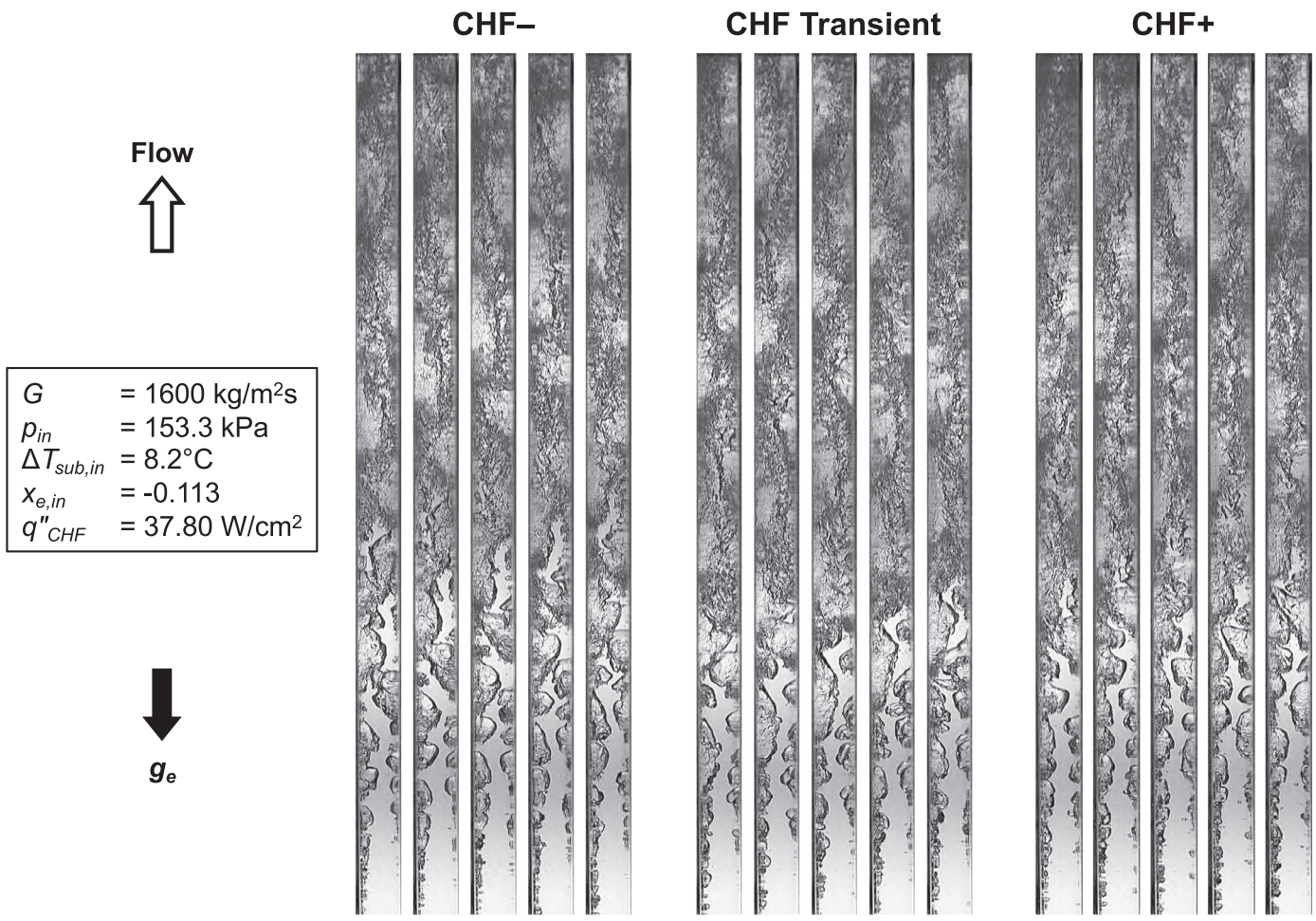

Fig. 5. Sequential images during CHF–, CHF transient, and CHF+ for G = 1600 kg/m^{2}s, p_{in} = 153.3 kPa, $\Delta T_{sub,in}$ = 8.2°C, $x_{e,in}$ = −0.113, and q''_{CHF} = 37.80 W/cm^2 with double-sided heating. The interval between successive images in all sequences is 1.5 ms.

within the channel compared to the double-sided in Fig. 6(b) for similar operating conditions.

Fig. 8(a) and (b) show experimental q''_{CHF} for a subset of a consolidated database, consisting of the new MST data, previously recorded data [32] for a variety of orientations, and microgravity data obtained during parabolic flight [34] (both single-sided and double-sided data were measured but only the latter previously published and analyzed). The previously recorded data are included to further evaluate the effectiveness of the *Interfacial Lift-off Model* in the upcoming section. The data are again segregated by inlet subcooling into either highly subcooled or near-saturated (using the same ranges of $\Delta T_{sub,in}$ as in Fig. 7(a) and (b)) and plotted against mass velocity. As expected, q''_{CHF} is shown to increase with increases in mass velocity and/or inlet subcooling. For each range of subcooling in both single-sided and double-sided heating, vertical upflow (indicated as 'up') yields the largest q''_{CHF} values. The vertical upflow orientation generally enhances q''_{CHF} by virtue of gravity aiding vapor removal from the heated wall and promoting liquid replenishment.

For single-sided heating, Fig. 8(a), horizontal flow with top-wall heating (indicated as 'top') resulted in the lowest q''_{CHF}. This can be readily explained by the buoyancy causing accumulation of an insulating vapor layer along the top wall. Notice how q''_{CHF} for each subcooling range follows a systematic order: highest for vertical upflow, followed by horizontal bottom-wall heating (indicated as 'bottom'), and horizontal top-wall heating. Interestingly, for the near-saturated cases, microgravity data are superior to those for horizontal top-wall heating, presumably because of the buoyancy induced vapor accumulation along the heated wall for the latter. Also, for the near-saturated cases, differences in q''_{CHF} among the two horizontal orientation and microgravity are more pronounced at lower mass velocities, where horizontal flow is very sensitive to buoyancy effects in the absence of strong inertial effects. However, there is gradual diminution of differences in q''_{CHF} with increasing mass velocity (as well as indication of convergence of values at the highest mass velocity tested) as inertia increasingly dominates over gravity and ultimately dwarfs gravity effects altogether.

Looking now at the double-sided heating configurations, Fig. 8(b), q''_{CHF} is shown to increase monotonically with increasing mass velocity. Fig. 8(b) included data for vertical downflow (indicated as 'down') as well. Here too, highest q''_{CHF} is achieved with vertical upflow. For the near-saturated range, horizontal flow shows lowest q''_{CHF} while microgravity data fall between those for vertical upflow and horizontal flow. The inferior performance for the horizontal orientation can be explained by the buoyancy promoting formation of an insulating vapor layer upon the top heated wall and triggering CHF along the same wall. For the highly subcooled range, there are no obvious advantages of horizontal flow versus vertical downflow, both being subject to adverse gravity effects, especially at lower mass velocities. However, q''_{CHF} for all flow orientations appear to converge at high mass velocities where inertia dominates any gravity effects. This observation has been utilized to identify gravity independence criteria for flow boiling and condensation in prior studies [40,41].

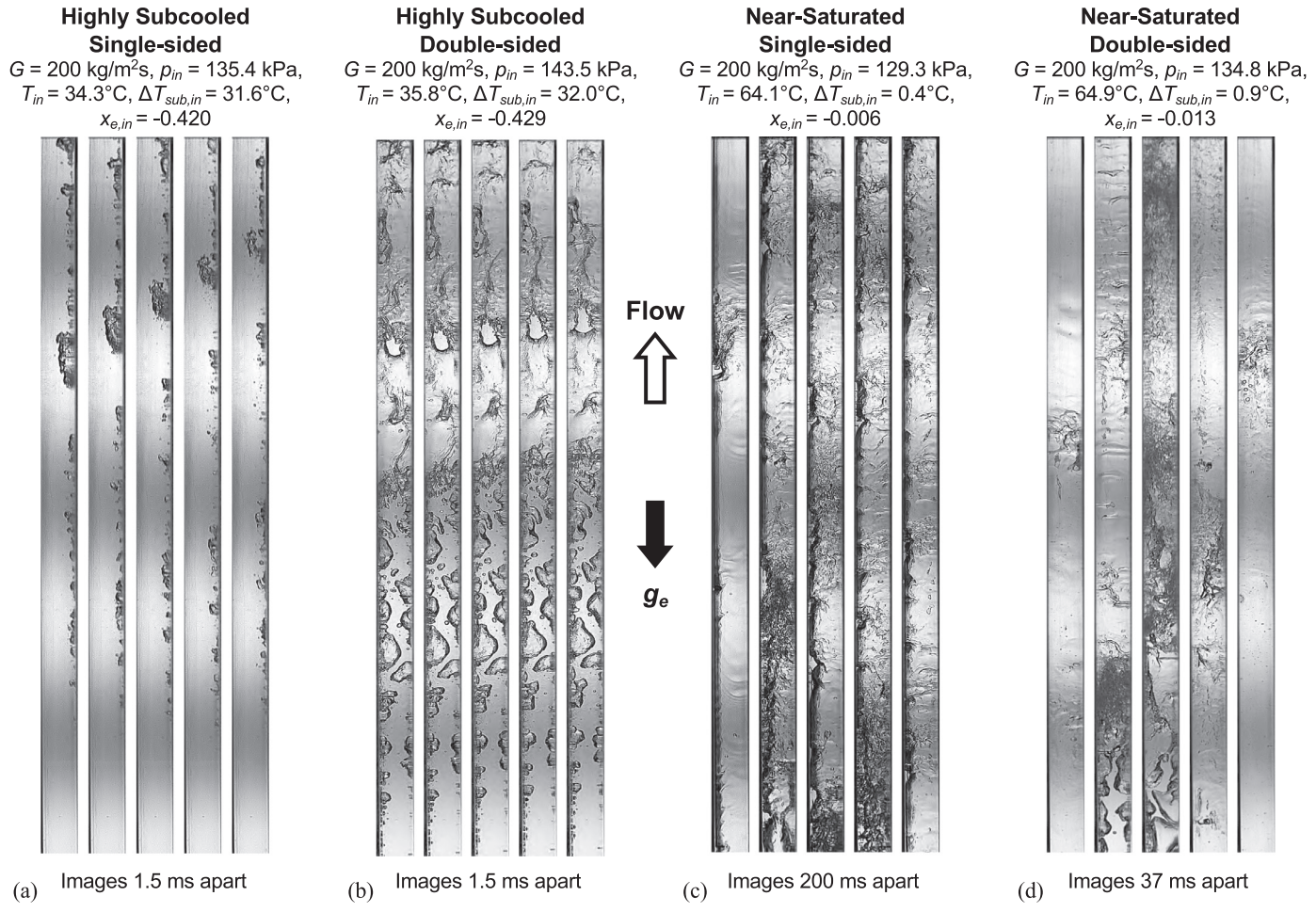

Fig. 6. Sequential images of CHF transient for $G = 200$ kg/m^{2}s and heating configurations of a) highly subcooled single-sided, b) highly subcooled double-sided, c) near-saturated single-sided, and d) near-saturated double-sided. Time interval between successive images is indicated below each sequence.

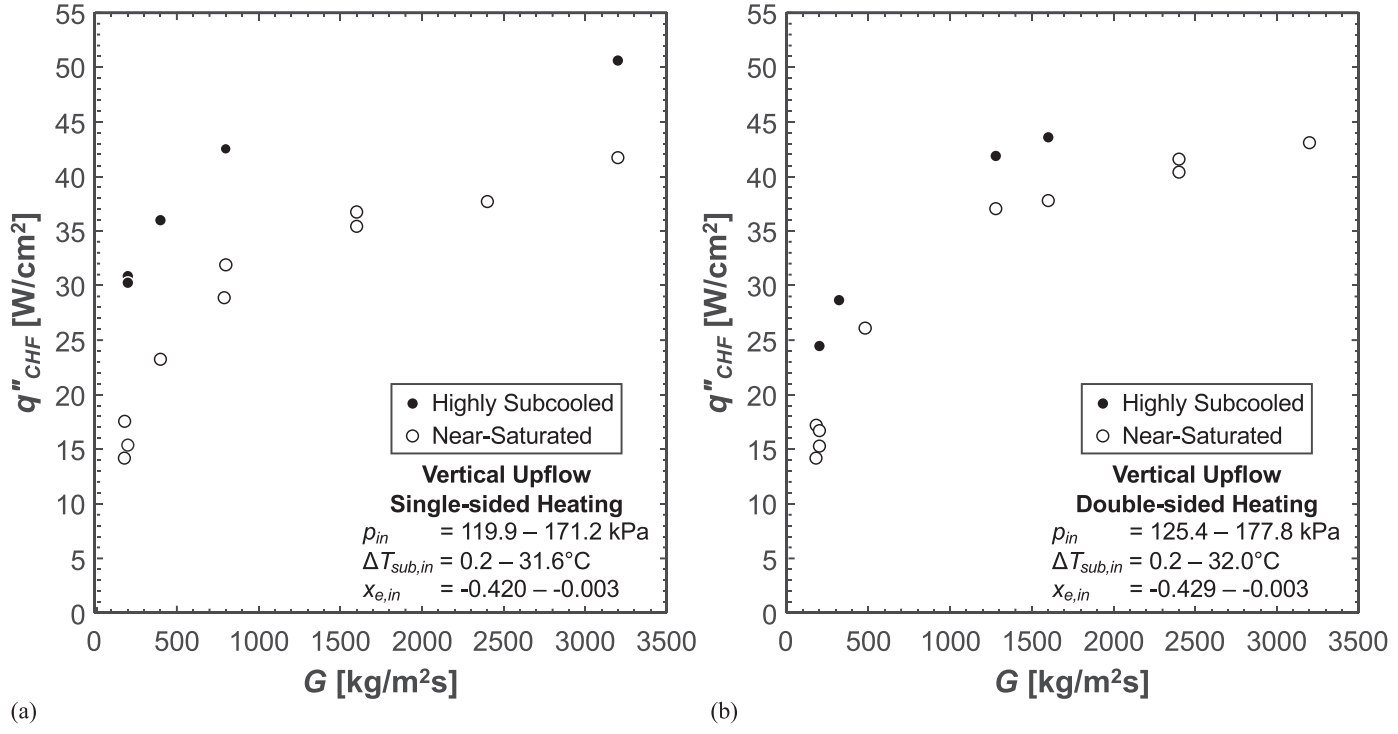

Fig. 7. MST Experimental CHF results for (a) single-sided heating and (b) double-sided heating.

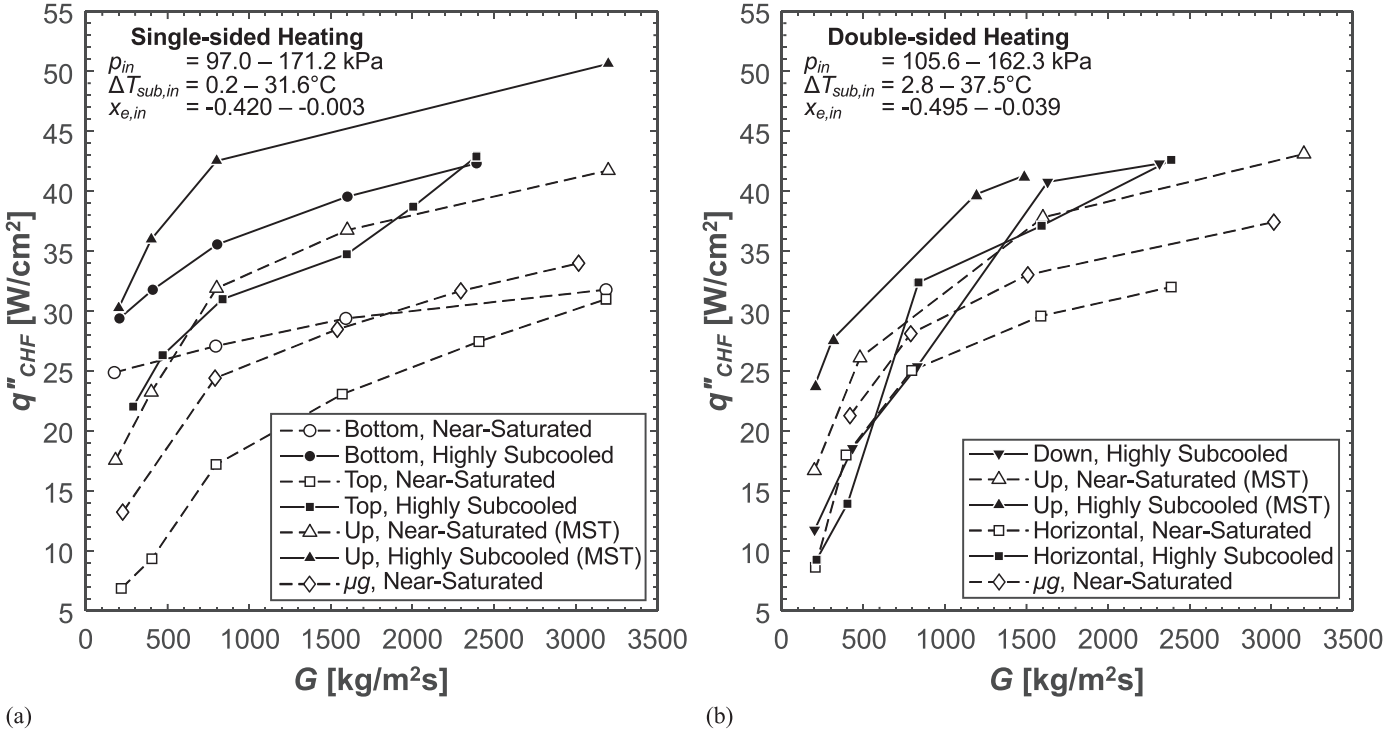

Fig. 8. Experimental CHF results for a subset of the consolidated database for (a) single-sided heating and (b) double-sided heating.

4. Interfacial lift-off model and predictions

4.1. Rationale

The *Interfacial Lift-off Model* is founded on visual evidence of channel flow boiling CHF provided in both the present study and numerous past studies for various combinations of heating configurations, inlet conditions, and gravitational environments [29,34,42–49]. The key feature found in each of these studies is the development of a continuous periodic wavy vapor layer that forms along the heated wall culminating in CHF. Prior to CHF, the vapor layer exists as distinct patches of vapor separated by wetting fronts which correspond to troughs in the wavy vapor layer. As CHF commences, the wetting fronts are extinguished, culminating in a continuous wavy vapor layer along the heated wall. The wavy form of the vapor layer is the result of a hydrodynamic instability between the two phases moving at different velocities. Visual observation shows intense boiling occurs within the wetting fronts during CHF-. It is postulated that CHF will occur when the momentum of vapor generated in the wetting fronts normal to the heated wall overcomes the pressure force generated (normal to and pointing toward the wall) by curvature of the interface. At this point, the wetting front is extinguished and heat that was initially removed within the wetting front is now transferred axially to the wetting fronts upstream, provoking their lift-off as well. Wetting fronts are therefore extinguished one after another in a chain reaction, causing the boiling process to be halted as a continuous vapor layer encapsulates the heated wall.

4.2. Model description

The methodology presented in the present paper aims to consolidate CHF predictions for subcooled inlet conditions. This section will give a brief overview of the modeling, assumptions, and equations used in the *Interfacial Lift-off Model*. This model has been previously employed to predict CHF for subcooled inlet conditions with single-sided heating [29] and double-sided heating [34]. The aim here is to consolidate predictions for both heating configurations and all levels of subcooling. Similar to the original model developed by Galloway and Mudawar [27,28], this model encompasses four sub-models which are used to calculate the heat flux required to trigger lift-off of the wetting fronts. Key equations of the model can be found in Table 2 for single-sided heating and Table 3 for double-sided heating, with additional details concerning momentum conservation for both are provided in Table 4.

First, a separated flow model is used to determine axial variations of key flow parameters that are utilized in subsequent sub-models. The following assumptions are made in derivation of the separated flow model: (1) the vapor layer is initiated at the leading edge of the heated wall, (2) velocity of each phase is uniform within the channel's cross-section, (3) pressure is uniform across the channel's entire cross-section, (4) vapor is maintained at the local saturation temperature, (5) vapor produced at the wetting front does not contribute to the streamwise momentum, and, (6) in the case of double-sided heating, equal heat flux is applied to each heated wall. Heating configuration dictates the number of control volumes examined in the separated flow model. A free body diagram of the control volumes of length Δz used in the model, and corresponding force and momentum terms are shown in Fig. 9 for single-sided heating and Fig. 10 for double-sided heating. For single-sided heating, one control volume is used for the vapor layer that forms along the heated wall, and another for the subcooled liquid. For double-sided heating, a control volume is required for each of the vapor layers that form along the opposite heated walls and another control volume for the subcooled liquid in the middle of the channel. Conservations of mass, momentum, and energy are used to determine axial variations in pressure, phase velocity, quality, and void fraction. Utilized within the conservation of energy is the *heat utility ratio,* ε, which is used to account for non-equilibrium effects caused by subcooling and better estimate the net amount of vapor being produced within the channel.

Table 2
Summary of equations used in the interfacial lift-off model for single-sided heating.

Conservation of momentum

$$G^2\frac{d}{dz}\left[\frac{x^2}{\rho_g\alpha}\right] = -\alpha\frac{dp}{dz} - \frac{\tau_{w,g}P_{w,g}}{A} \pm \frac{\tau_i P_i}{A} - \rho_g\alpha g\sin\theta$$

$$G^2\frac{d}{dz}\left[\frac{(1-x)^2}{\rho_b(1-\alpha)}\right] = -(1-\alpha)\frac{dp}{dz} - \frac{\tau_{w,b}P_{w,b}}{A} \mp \frac{\tau_i P_i}{A} - \rho_b(1-\alpha)g\sin\theta$$

Local velocity

$$u_g = \frac{xG}{\rho_g\alpha};\ u_f = \frac{(1-x)G}{(1-\alpha)\rho_b}$$

Conservation of energy

$$\frac{dx}{dz} = \frac{\varepsilon q''_w W}{GA\left[h_{fg}(z)+\Delta h_{sub}\right]}$$

$$h_b = \frac{h_{in} - xh_g + \frac{q''_w P_h}{GA}z}{(1-x)}$$

Critical wavelength

$$k_c = \frac{2\pi}{\lambda_c} = \frac{\rho''_b\rho''_g(u_g-u_f)^2}{2\sigma(\rho''_b+\rho''_g)} + \sqrt{\left[\frac{\rho''_b\rho''_g(u_g-u_f)^2}{2\sigma(\rho''_b+\rho''_g)}\right]^2 + \frac{(\rho_b-\rho_g)g_n}{\sigma}}$$

where $\rho''_b = \rho_b\coth(k(H-\delta))$ and $\rho''_g = \rho_g\coth(k\delta)$

Lift-off criteria

$$q''_{CHF} = \begin{cases} \frac{\rho_g}{\varepsilon}(c_{p,f}\Delta T_{sub,out} + h_{fg})\left[\frac{4\pi\sigma b}{\rho_g}\sin(\pi b)\right]^{0.5}\frac{\delta^{0.5}}{\lambda_c}\Big|_{z^*}, & x_{e,out} < 0 \\ \rho_g(c_{p,f}\Delta T_{sub,in} + h_{fg})\left[\frac{4\pi\sigma b}{\rho_g}\sin(\pi b)\right]^{0.5}\frac{\delta^{0.5}}{\lambda_c}\Big|_{z^*}, & x_{e,out} \geq 0 \end{cases}$$

Heat utility ratio

$$\varepsilon = 1 - 0.00285\frac{\rho_f}{\rho_g}\frac{c_{p,f}\Delta T_{sub,out}}{h_{fg}}\left(\frac{\rho_f u_{in}^2 D}{\sigma}\right)$$

Table 3
Summary of equations used in the interfacial lift-off model for double-sided heating.

Conservation of momentum

$$G^2\frac{d}{dz}\left[\frac{x_1^2}{\rho_g\alpha_1}\right] = -\alpha_1\frac{dp}{dz} - \frac{\tau_{w,g1}P_{w,g1}}{A} \pm \frac{\tau_{i1}P_{i1}}{A} - \rho_g\alpha_1 g\sin\theta$$

$$G^2\frac{d}{dz}\left[\frac{x_2^2}{\rho_g\alpha_2}\right] = -\alpha_2\frac{dp}{dz} - \frac{\tau_{w,g2}P_{w,g2}}{A} \pm \frac{\tau_{i2}P_{i2}}{A} - \rho_g\alpha_2 g\sin\theta$$

$$G^2\frac{d}{dz}\left[\frac{(1-x_1-x_2)^2}{\rho_b(1-\alpha_1-\alpha_2)}\right] = -(1-\alpha_1-\alpha_2)\frac{dp}{dz} - \frac{\tau_{w,b}P_{w,b}}{A} \mp \frac{\tau_{i1}P_{i1}}{A} \mp \frac{\tau_{i2}P_{i2}}{A} - \rho_b(1-\alpha_1-\alpha_2)g\sin\theta$$

Local velocity

$$u_{g1} = \frac{x_1 G}{\rho_g\alpha_1};\ u_{g2} = \frac{x_2 G}{\rho_g\alpha_2};\ u_f = \frac{(1-x_1-x_2)G}{(1-\alpha_1-\alpha_2)\rho_b}$$

Conservation of energy

$$\frac{dx_1}{dz} = \frac{dx_2}{dz} = \frac{\varepsilon q''_w W}{GA\left[h_{fg}(z)+\Delta h_{sub}\right]}$$

$$h_b = \frac{h_{in} - (x_1+x_2)h_g + \frac{q''_w P_h}{GA}z}{(1-x_1-x_2)}$$

Critical wavelength

$$k_{c1} = \frac{2\pi}{\lambda_{c1}} = \frac{\rho''_b\rho''_{g1}(u_{g1}-u_f)^2}{2\sigma(\rho''_b+\rho''_{g1})} + \sqrt{\left[\frac{\rho''_b\rho''_{g1}(u_{g1}-u_f)^2}{2\sigma(\rho''_b+\rho''_{g1})}\right]^2 + \frac{(\rho_b-\rho_g)g_{n1}}{\sigma}}$$

$$k_{c2} = \frac{2\pi}{\lambda_{c2}} = \frac{\rho''_b\rho''_{g2}(u_{g2}-u_f)^2}{2\sigma(\rho''_b+\rho''_{g2})} + \sqrt{\left[\frac{\rho''_b\rho''_{g2}(u_{g2}-u_f)^2}{2\sigma(\rho''_b+\rho''_{g2})}\right]^2 + \frac{(\rho_b-\rho_g)g_{n2}}{\sigma}}$$

where $\rho''_{g1} = \rho_g\coth(k\delta_1)$, $\rho''_{g2} = \rho_g\coth(k\delta_2)$, $\rho''_b = \rho_b\coth(k(H-\delta_1-\delta_2))$, $g_{n1} = g\cos(\theta+\pi) = -g\cos\theta$, and $g_{n2} = g\cos\theta$

Lift-off criteria

$$q''_{CHF,a} = \begin{cases} \frac{\rho_g}{\varepsilon}(c_{p,f}\Delta T_{sub,out} + h_{fg})\left[\frac{4\pi\sigma b}{\rho_g}\sin(\pi b)\right]^{0.5}\frac{\delta_a^{0.5}}{\lambda_{ca}}\Big|_{z^*}, & x_{e,out} < 0 \\ \rho_g(c_{p,f}\Delta T_{sub,in} + h_{fg})\left[\frac{4\pi\sigma b}{\rho_g}\sin(\pi b)\right]^{0.5}\frac{\delta_a^{0.5}}{\lambda_{ca}}\Big|_{z^*}, & x_{e,out} \geq 0 \end{cases}$$

Heat utility ratio

$$\varepsilon = 1 - 0.00285\frac{\rho_f}{\rho_g}\frac{c_{p,f}\Delta T_{sub,out}}{h_{fg}}\left(\frac{\rho_f u_{in}^2 D}{\sigma}\right)$$

Table 4
Summary of expressions used in conservation of momentum.

Wall shear stress [53]
$\tau_{w,k} = \frac{1}{2}\rho_k u_k f_k$
Wall friction factor
$f_k = C_1 + \frac{C_2}{Re_k^{1/C_3}}$
Phase Reynolds number
$Re_k = \frac{\rho_k u_k D_k}{\mu_k}$
Friction factor constants for laminar flow ($Re_k \leq 2100$)
$C_1 = 0$; $C_2 = 16$; $C_3 = 1$
Friction factor constants for transitional flow ($2100 < Re_k \leq 4000$)
$C_1 = 0.0054$; $C_2 = 2.3 \times 10^{-8}$; $C_3 = -2/3$
Friction factor constants for turbulent flow ($Re_k > 4000$)
$C_1 = 0.00128$; $C_2 = 0.1143$; $C_3 = 3.2154$
Interfacial shear stress
$\tau_{i1} = C_{f,i}\rho_g(u_{g1} - u_f)^2$ and $\tau_{i2} = C_{f,i}\rho_g(u_{g2} - u_f)^2$ where $C_{f,i} = 0.5$ [28]

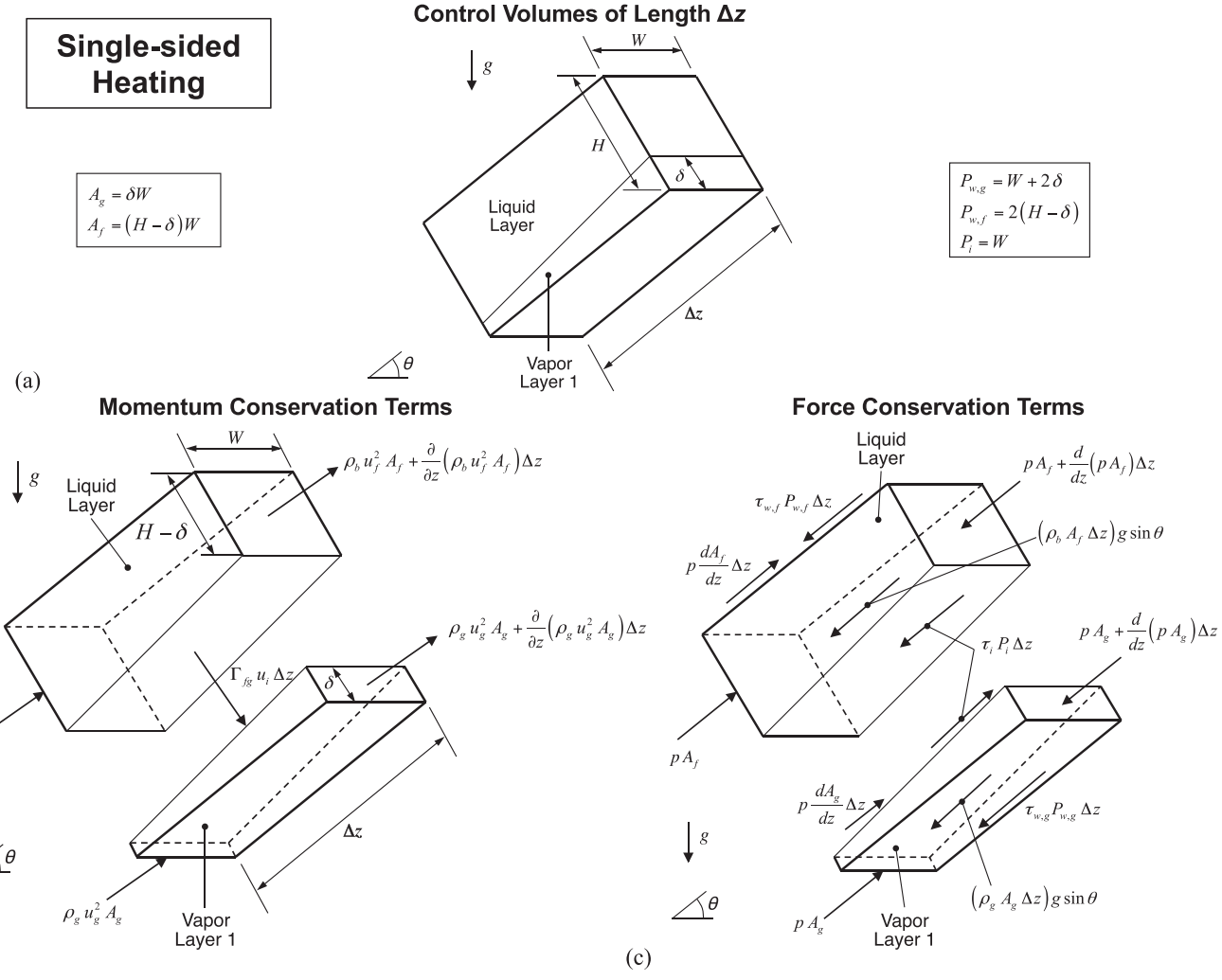

Fig. 9. Separated flow modeling of single-sided heating configuration: (a) control volumes of length Δz, (b) momentum terms for individual layers, and (c) force terms for individual layers.

Classical instability theory [28,50,51] is applied to describe the interface of two fluids moving at different velocities as an ideal sinusoid. Schematics of the development of interface as well as the modeled sinusoid used in instability analysis are respectively depicted in Fig. 11(a) and (b) for double-sided heating. In the case of single-sided heating, the interface between liquid and vapor is modeled identically to double-sided heating, however only a single interface is present. The stability of the interface is determined by the relative magnitudes of inertia, surface tension, and body force. In microgravity, body force will have a negligible role in determining critical wavelength, λ_c, and in the case of double-sided heating, the interface along both walls will have the same wavelength. Furthermore, the effects of gravity are not lost between the vertical orientations in Earth gravity and in microgravity. Al-

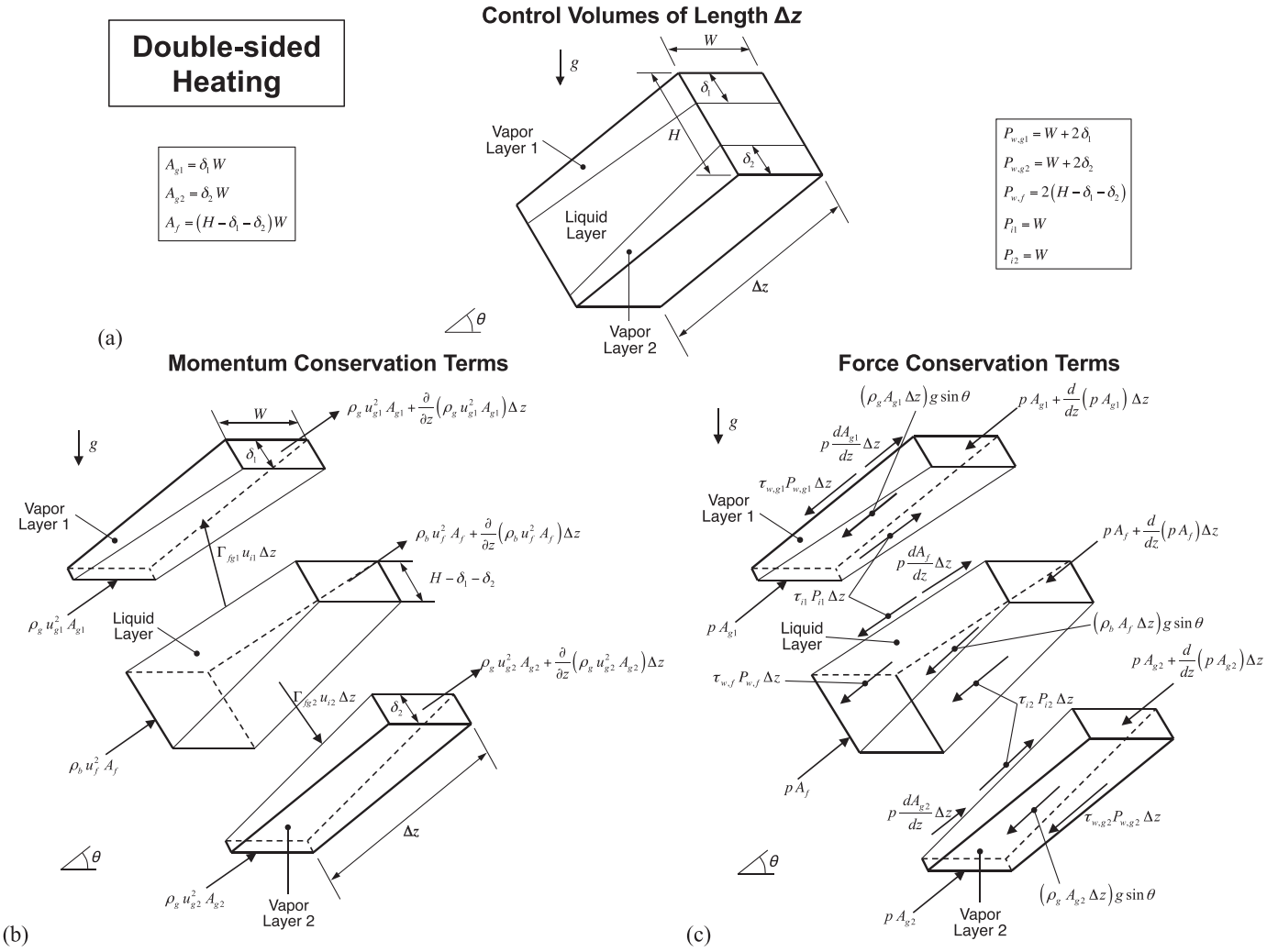

Fig. 10. Separated flow modeling of double-sided heating configuration: (a) control volumes of length Δz, (b) momentum terms for individual layers, and (c) force terms for individual layers.

though the gravity components perpendicular to the wall get nullified in the λ_c equation, the gravity component parallel to the wall is non-zero and impacts the estimation of both local pressure and void fraction in the conservation of momentum equations, which in turn alters the thermophysical properties, vapor layer thickness, modified density, and finally λ_c. For instance, λ_c for vertical upflow and downflow is expected to be respectively smaller and larger than in microgravity. The first goal of stability analysis is to determine critical wavelength of the interface. The critical wavelength is that which triggers instability of the interface. An unstable interface is necessary to allow the interface to contact the heated wall and form wetting fronts. The stability analysis is also used to determine the interfacial curvature and its associated pressure force which holds wetting fronts against the heated wall.

CHF is triggered once the momentum of vapor normal to the wall in the wetting front exceeds the pressure force associated with interfacial curvature. Comparing the two requires knowledge of axial span – length – of the wetting front. Sturgis and Mudawar [30] analyzed the wavy vapor layer prior to CHF and found the length of wetting front to be a constant fraction of the wavelength, $b\lambda$, where $b = 0.2$. The heat flux required to induce interfacial lifting of the wetting front is found by relating the velocity of vapor generated in the wetting front to the momentum of vapor required to initiate the lift-off.

A simple energy balance is then used to relate the heat flux supplied from the wall and the heat flux concentrated in the wetting fronts. The instability analysis, lift-off criterion, and wall energy balance are combined to yield the final relation for q''_{CHF}. The final formulation of CHF is segregated into saturated or subcooled conditions, with differences between the two formulations stemming from observations and assumptions used in previous versions of the model. Zhang *et al.* [44] observed that CHF is initiated at the furthest downstream wetting front. For subcooled CHF, $x_{e,out} < 0$, and outlet subcooling is used to account for appreciable axial variations in subcooling. The non-equilibrium effects stemming from subcooling are accounted for in the *heat utility ratio*. However, for saturated CHF cases, $x_{e,out} \geq 0$, and inlet subcooling is considered instead. Konishi *et al.* [34] considered test cases with relatively low inlet subcooling and assumed that the liquid phase preserves its subcooling in the axial direction. This assumption was applied to saturated CHF cases where non-equilibrium effects are miniscule and the heat utility ratio is equal to unity, which indicates vaporization of the fluid utilizes the entirety of the applied heat flux.

4.3. Model procedure

The model is iterative in its procedure and is initiated by guessing a q''_{CHF}. The separated flow model with the assumed q''_{CHF} coupled with a fourth-order Runga-Kutta numerical scheme deter-

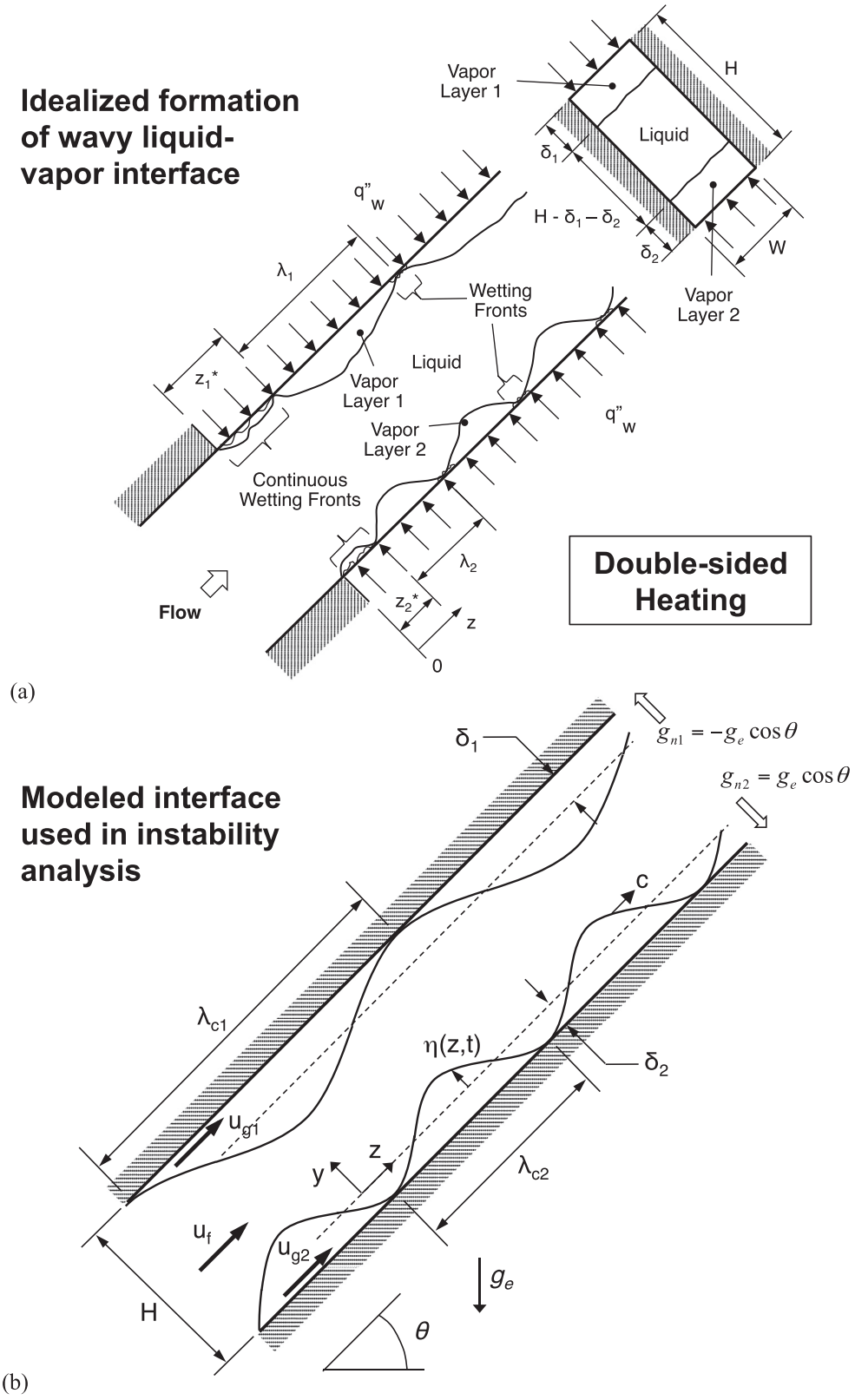

Fig. 11. Schematics of the (a) idealized formation of wavy liquid-vapor interface and (b) modeled interface used in instability analysis in a terrestrial environment.

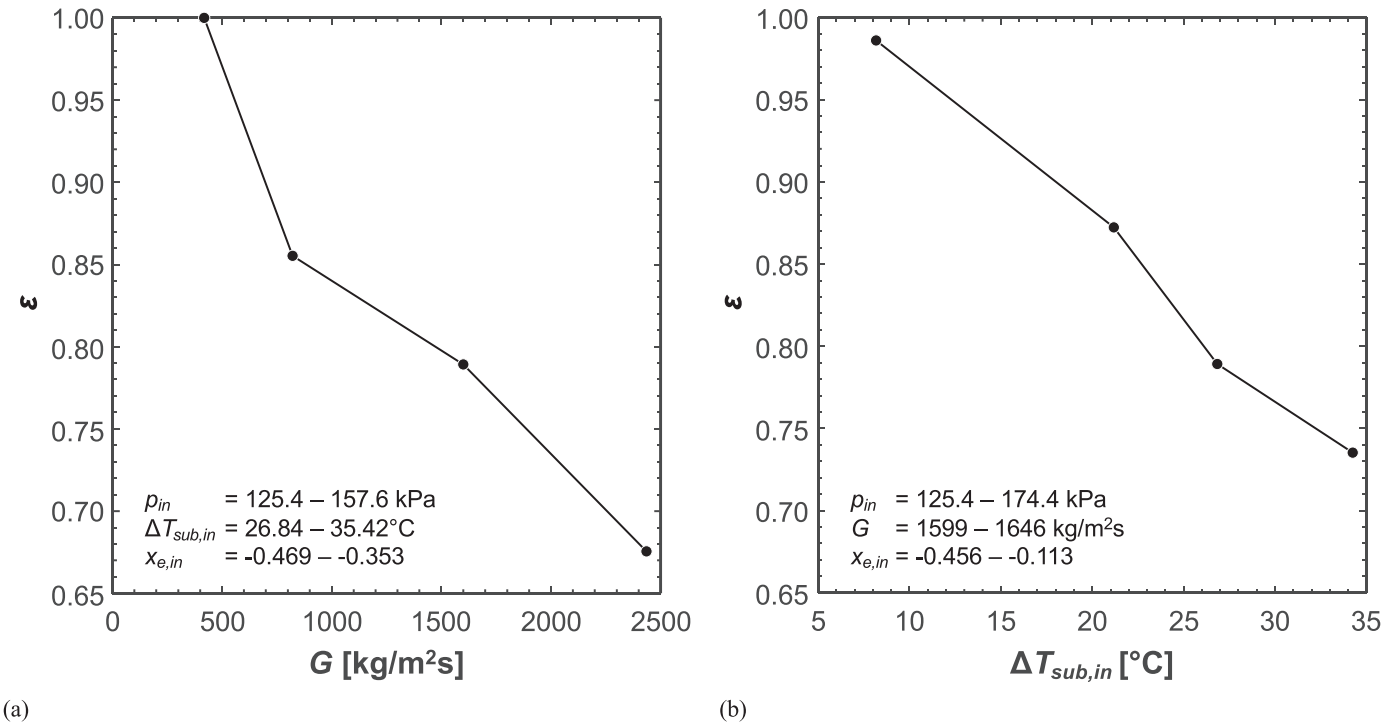

Fig. 12. Predicted heat utility ratio for different values of (a) mass velocity and (b) inlet subcooling.

mines local flow properties along the heated length of the channel. The separated flow model is used to determine axial z_o where velocity of the vapor phase just surpasses that of liquid core. Next, a critical wavelength, λ_c, is assumed and the separated flow model is called upon again to determine the flow properties at z^* which is defined as $z^* = z_o + \lambda_c$ and marks the end of the upstream continuous wetting region prior to the formation of wetting fronts. At z^*, a new critical wavelength is calculated which is dependent on flow properties and vapor phase thickness at z^*. This method is iterative until the assumed critical wavelength matches the calculated value. Once the critical wavelength is determined, q''_{CHF} is calculated using the equation for q''_{CHF} evaluated at z^*. The entire process is repeated until the assumed heat flux converges to the calculated q''_{CHF}. In the case of double-sided heating, the process is repeated for each heated wall and the minimum q''_{CHF} value between the two walls is deemed the true q''_{CHF}.

4.4. Predicted heat utility ratio trends

One of the key parameters of the model is the heat utility ratio, ε. This parameter is used to determine the fraction of the wall heat flux which is devoted to liquid vaporization, and is especially important for subcooled conditions where exit equilibrium quality is less than 0. Fig. 12(a) and (b) show variations of predicted heat utility ratio at CHF with mass velocity and inlet subcooling, respectively. Fig. 12(a) shows ε decreases monotonically with increasing mass velocity, a trend that can be explained by increased effectiveness in utilizing sensible heat of near-wall liquid, while causing faster removal of core liquid from the heated region length of the channel before having sufficient time to vaporize. Fig. 12(b) shows a somewhat similar trend of ε with inlet subcooling. The monotonic decrease in this case is mostly the result of increased sensible heat content of the fluid. These trends demonstrate the importance of incorporating the effects of heat utility ratio when using the CHF model; absent these effects, the model would likely overpredict the amount of vapor produced in the channel. The parametric trends observed from the model predictions conform the dependence of ε dependence in Tables 2 and 3 on outlet subcooling. In either case, with higher inlet subcooling or mass velocity, higher outlet subcooling would be expected, resulting in lower ε. The equations for q''_{CHF} in the same table indicate q''_{CHF} is inversely proportional to ε. This aligns with the observed experimental trends that increasing inlet subcooling or mass velocity, which tend to decrease ε, also yield higher q''_{CHF}.

4.5. Comparison of CHF model predictions and experimental data

Fig. 13(a) and (b) compare q''_{CHF} predicted by the *Interfacial Lift-off Model* to values from the consolidated experimental database for single- and double-sided heating, respectively. For each of the two configurations, only a subset of the total database is used for comparisons with the model. As mentioned previously, the model is based on presence of a wavy liquid-vapor interface that creates wetting fronts along the channel. Visual evidence has shown that the required interface is not present at low mass velocities and the analytical model is prone to break down at these conditions. This is consistent with previous observations made regarding the *Interfacial Lift-off Model* for different mass velocities and flow orientations [52]. It is therefore important when using the model to clearly identify boundaries for operating conditions where the wavy vapor layer is present. Table 5 shows the range of operating conditions used for comparison as well as the limitations set from visual evidence provided in this paper along with recommendations provided in previous papers [42,52]. The predictive accuracy of each model is determined by calculating using mean absolute error, *MAE*. With N data points, the *MAE* is calculated according to

$$MAE(\%) = \frac{1}{N}\sum \left| \frac{q''_{CHF,pred} - q''_{CHF,exp}}{q''_{CHF,exp}} \right| \times 100. \quad (6)$$

Fig. 13(a) shows q''_{CHF} for single-sided heating is predicted with a *MAE* of 18.98% (for $N = 38$) with 81.58% of datapoints predicted within ±30%. Fig. 13(b) shows a *MAE* of 19.07% (for $N = 54$) for double-sided heating with 87.04% of datapoints predicted within

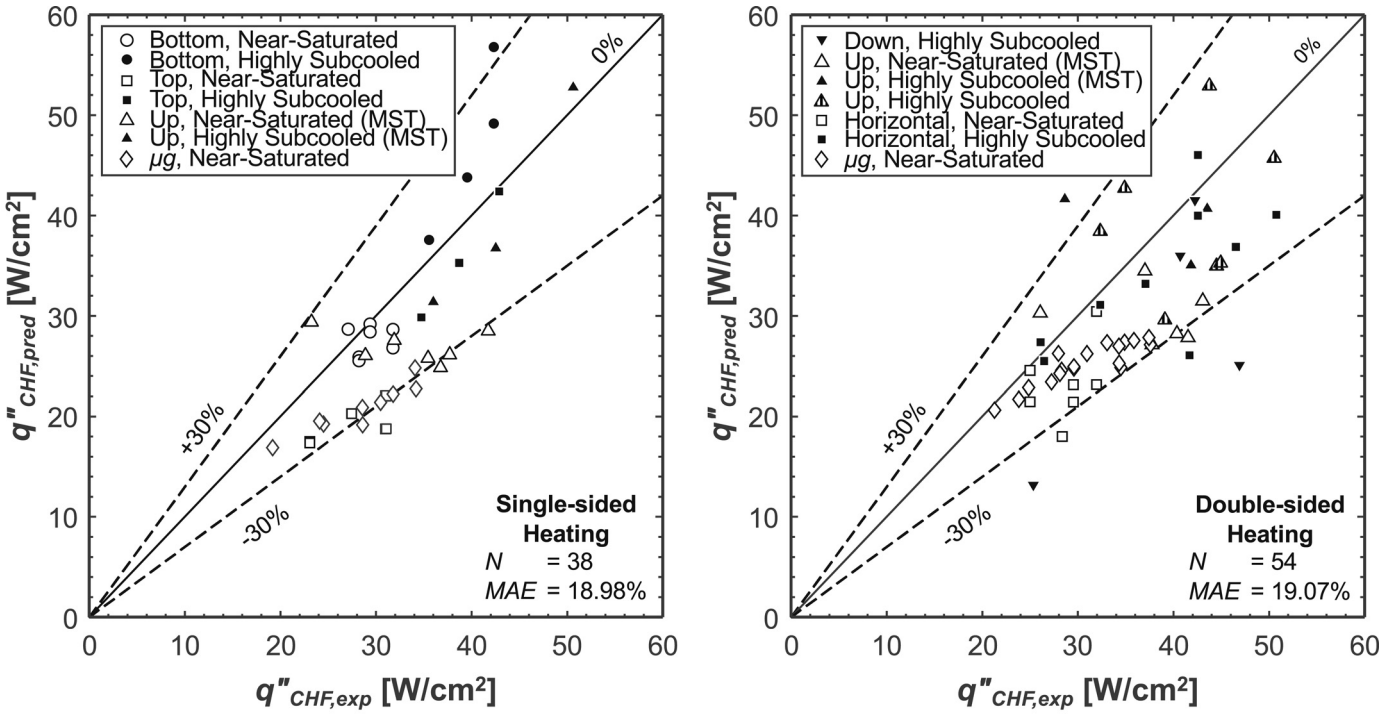

Fig. 13. Comparison of experimental and predicted CHF values for (a) single-sided heating and (b) double-sided heating.

Table 5
Summary of operating conditions used for CHF predictions.

Configuration	G [kg/m^{2}s]	p_{in} [kPa]	T_{in} [°C]	$\Delta T_{sub,in}$ [°C]	$x_{e,in}$	Orientation	Limitation
Single	794 – 3199	99.0 – 161.8	29.9 – 66.9	3.9 – 28.3	−0.362 – −0.054	Horizontal Bottom	u_{in} > 0.5 m/s
Single	1570 – 3200	100.1 – 161.5	29.8 – 67.2	3.6 – 28.4	−0.363 – −0.048	Horizontal Top	u_{in} > 1.0 m/s
Single	400 – 3200	119.9 – 171.2	36.6 – 71.6	0.5 – 28.0	−0.380 – −0.007	Up	u_{in} > 0.15 m/s
Single (μg)	420 – 3019	122.4 – 150.0	58.8 – 63.4	3.6 – 5.9	−0.081 – −0.049	Up	u_{in} > 0.15 m/s
Double	793 – 2409	100.2 – 165.8	27.6 – 64.7	4.9 – 33.2	−0.435 – −0.065	Horizontal	u_{in} > 0.5 m/s
Double	320 – 3200	125.4 – 190.8	28.9 – 73.0	3.7 – 35.4	−0.467 – −0.051	Up	u_{in} > 0.15 m/s
Double	831 – 2314	130.6 – 179.7	27.9 – 51.6	23.6 – 37.5	−0.495 – −0.330	Down	u_{in} > 0.5 m/s
Double (μg)	391 – 3050	109.8 – 166.8	51.0 – 65.5	1.9 – 9.6	−0.125 – −0.025	Up	u_{in} > 0.15 m/s

±30%. These statistics reflect good predictive capability for both heating configurations and all mass velocities yielding wavy vapor layer behavior.

As mentioned earlier, one of the main driving forces of the instability causing the wavy liquid-vapor interface is the velocity difference between the two phases. At very low mass velocities, the influence of velocity difference is too weak to overcome the relatively small stabilizing effect of surface tension. Other notable cases in Table 5 that have higher mass velocity cut offs are horizontal flow with top wall heating and vertical downflow. For the former, strong transverse influence of buoyancy causes vapor to congregate along the top wall preventing formation of wetting fronts along the top heated wall. And in the case of vertical downflow, buoyancy acts opposite the flow direction, weakening inertial and shear forces exerted upon the vapor and resulting at times in vapor stagnation and even vapor counterflow at low mass velocities. These regimes do not exhibit the wavy vapor layer behavior necessary for implementing the *Interfacial Lift-off Model*.

5. Conclusions

This study aimed to investigate CHF for subcooled-inlet flow boiling of nPFH based on results of pre-launch Earth-gravity Mission Sequence Tests (MSTs) of NASA's Flow Boiling and Condensation Experiment (FBCE), which was launched to the International Space Station (ISS) in August 2021. The CHF measurements were performed in FBCE's Flow Boiling Module (FBM) in the vertical upflow orientation with both single-sided and double-sided heating. The MST data was combined with data recorded during previous ground tests (conducted at different orientations with respect to Earth gravity) and parabolic flight microgravity tests to form a consolidated subcooled-inlet FBCE-CHF database. The *Interfacial Lift-off Model* was carefully assessed for predictive accuracy by comparing predictions to the consolidated database. Key conclusions from the study are:

(1) Experimental parametric trends of CHF were investigated for both single-sided and double-sided heating configurations. CHF was observed to increase with increases in mass velocity and/or inlet subcooling. These trends were accurately captured by formulations of *heat utility ratio* incorporated in the *Interfacial Lift-off Model*.
(2) Analysis of high-speed video image sequences confirmed the formation of a wavy vapor layer leading up to CHF, with liquid access to the heated wall available only in wetting fronts corresponding to the wave toughs. And CHF was triggered when intense vapor production in the wetting fronts caused the interface to lift off the heated wall, culminating in a fairly continuous insulating wavy vapor layer encasing the entire heated wall.

However, other interfacial behaviors and CHF trigger mechanisms were also observed, especially for combinations of low mass velocity, horizontal flow with top wall heating, and vertical downflow. These conditions were excluded from assessment of the *Interfacial Lift-off Model*.

(3) The interfacial lift-off model showed good accuracy in predicting q''_{CHF} of both single-sided and double-sided heating for broad ranges of mass velocity and inlet subcooling, different flow orientations in Earth gravity, and flow boiling in microgravity.

Declaration of Competing Interest

The authors declare that they have no known competing financial interests or personal relationships that could have appeared to influence the work reported in this paper.

Acknowledgement

The authors are grateful for the support of the National Aeronautics and Space Administration under grant no. NNX17AK98G. The authors thank the team at NASA Glenn Research Center, especially Nancy Hall (FBCE Project Manager), Rochelle May and Phillip Gonia (Software Engineering), Mark Sorrells (Assembly, Integration and Test Lead), Jesse DeFiebre (Fluids Lead), Monica Guzik (FBCE Chief Engineer), and ZIN FCF Mission Operations Team for their dedicated technical support and the successful Mission Sequence Test.

References

[1] F.P. Chiaramonte, J.A. Joshi, Workshop on critical issues in microgravity fluids, transport, and reaction processes in advanced human support technology – final report, NASA TM-2004-212940, 2004.
[2] The National AcademiesRecapturing a Future for Space Exploration, National Academies Press, Washington, D.C., USA, 2011, doi:10.17226/13048.
[3] T.J. LaClair, I. Mudawar, Thermal transients in a capillary evaporator prior to the initiation of boiling, Int. J. Heat Mass Transfer 43 (21) (2000) 3937–3952, doi:10.1016/S0017-9310(00)00042-9.
[4] G. Liang, I. Mudawar, Review of pool boiling enhancement by surface modification, Int. J. Heat Mass Transfer 128 (2019) 892–933, doi:10.1016/j.ijheatmasstransfer.2018.09.026.
[5] I. Mudawar, R.A. Houpt, Mass and momentum transport in smooth falling liquid films laminarized at relatively high Reynolds numbers, Int. J. Heat Mass Transfer 36 (14) (1993) 3437–3448, doi:10.1016/0017-9310(93)90162-Y.
[6] C.O. Gersey, I. Mudawar, Effects of heater length and orientation on the trigger mechanism for near-saturated flow boiling critical heat flux—I. Photographic study and statistical characterization of the near-wall interfacial features, Int. J. Heat Mass Transfer 38 (4) (1995) 629–641, doi:10.1016/0017-9310(94)00193-Y.
[7] S. Mukherjee, I. Mudawar, Pumpless loop for narrow channel and microchannel boiling, J. Electron. Packag. 125 (3) (2003) 431–441, doi:10.1115/1.1602708.
[8] S. Lee, V.S. Devahdhanush, I. Mudawar, Pressure drop characteristics of large length-to-diameter two-phase micro-channel heat sinks, Int. J. Heat Mass Transfer 115 (2017) 1258–1275, doi:10.1016/j.ijheatmasstransfer.2017.08.104.
[9] J. Lee, S.J. Darges, I. Mudawar, Experimental investigation and analysis of parametric trends of instability in two-phase micro-channel heat sinks, Int. J. Heat Mass Transfer 170 (2021) 120980, doi:10.1016/j.ijheatmasstransfer.2021.120980.
[10] W.P. Klinzing, J.C. Rozzi, I. Mudawar, Film and transition boiling correlations for quenching of hot surfaces with water sprays, J. Heat Treat. 9 (2) (1992) 91–103, doi:10.1007/BF02833145.
[11] M.E. Johns, I. Mudawar, An ultra-high power two-phase jet-impingement avionic clamshell module, J. Electron. Packag. 118 (4) (1996) 264–270, doi:10.1115/1.2792162.
[12] V.S. Devahdhanush, I. Mudawar, Critical heat flux of confined round single jet and jet array impingement boiling, Int. J. Heat Mass Transfer 169 (2021) 12–14, doi:10.1016/j.ijheatmasstransfer.2020.120857.
[13] M.K. Sung, I. Mudawar, Correlation of critical heat flux in hybrid jet impingement/micro-channel cooling scheme, Int. J. Heat Mass Transfer 49 (15–16) (2006) 2663–2672, doi:10.1016/j.ijheatmasstransfer.2006.01.008.
[14] T. Oka, Y. Abe, Y.H. Mori, A. Nagashima, Pool boiling of n-pentane, CFC-113, and water under reduced gravity: parabolic flight experiments with a transparent heater, J. Heat Transfer 117 (2) (1995) 408–417, doi:10.1115/1.2822537.
[15] W.M. Rohsenow, A Method of Correlating Heat Transfer Data For Surface Boiling of Liquids, Technical Report 5, Division of Industrial Cooperation, Massachusetts Institute of Technology, Cambridge, MA, USA, 1951.
[16] S. Levy, Prediction of the critical heat flux in forced convection flow, report GEAP-3961, General Electric Company Atomic Power Equipment Department, San Jose, CA, USA, 1962, doi:10.2172/4704320.
[17] W. Gambill, Generalized prediction of burnout heat flux for flowing, subcooled, wetting liquids, Chem. Eng. Prog. Symp. Ser. 59 (41) (1963) 71–87.
[18] V.S. Devahdhanush, S. Lee, I. Mudawar, Experimental investigation of subcooled flow boiling in annuli with reference to thermal management of ultra-fast electric vehicle charging cables, Int. J. Heat Mass Transfer 172 (2021) 121176, doi:10.1016/j.ijheatmasstransfer.2021.121176.
[19] S. Lee, V.S. Devahdhanush, I. Mudawar, Investigation of subcooled and saturated boiling heat transfer mechanisms, instabilities, and transient flow regime maps for large length-to-diameter ratio micro-channel heat sinks, Int. J. Heat Mass Transfer 123 (2018) 172–191, doi:10.1016/j.ijheatmasstransfer.2018.02.020.
[20] V. Prodanovic, D. Fraser, M. Salcudean, On the transition from partial to fully developed subcooled flow boiling, Int. J. Heat Mass Transfer 45 (24) (2002) 4727–4738, doi:10.1016/S0017-9310(02)00197-7.
[21] P. Saha, N. Zuber, Point of net vapor generation and vapor void fraction in subcooled boiling, in: Proc. Int. Heat Transfer Conf. 5, Begellhouse, Tokyo, Japan, 1974, pp. 175–179, doi:10.1615/IHTC5.430.
[22] D.D. Hall, I. Mudawar, Critical heat flux (CHF) for water flow in tubes-II. Subcooled CHF correlations, Int. J. Heat Mass Transfer 43 (14) (2000) 2605–2640, doi:10.1016/S0017-9310(99)00192-1.
[23] D.D. Hall, I. Mudawar, Critical heat flux (CHF) for water flow in tubes-I. Compilation and assessment of world CHF data, Int. J. Heat Mass Transfer 43 (14) (2000) 2573–2604, doi:10.1016/S0017-9310(99)00191-X.
[24] S.S. Kutateladze, A.I. Leont'ev, Some applications of the asymptotic theory of the turbulent boundary layer, in: Proc. Int. Heat Transfer Conf. 3, Begellhouse, Chicago, IL, USA, 1966, pp. 1–6, doi:10.1615/IHTC3.1920.
[25] J. Weisman, B.S. Pei, Prediction of critical heat flux in flow boiling at low qualities, Int. J. Heat Mass Transfer 26 (10) (1983) 1463–1477, doi:10.1016/S0017-9310(83)80047-7.
[26] C.H. Lee, I. Mudawwar, A mechanistic critical heat flux model for subcooled flow boiling based on local bulk flow conditions, Int. J. Multiphase Flow 14 (6) (1988) 711–728, doi:10.1016/0301-9322(88)90070-5.
[27] J.E. Galloway, I. Mudawar, CHF mechanism in flow boiling from a short heated wall—I. Examination of near-wall conditions with the aid of photomicrography and high-speed video imaging, Int. J. Heat Mass Transfer 36 (10) (1993) 2511–2526, doi:10.1016/S0017-9310(05)80190-5.
[28] J.E. Galloway, I. Mudawar, CHF mechanism in flow boiling from a short heated wall—II. Theoretical CHF model, Int. J. Heat Mass Transfer 36 (10) (1993) 2527–2540, doi:10.1016/S0017-9310(05)80191-7.
[29] H. Zhang, I. Mudawar, M.M. Hasan, CHF model for subcooled flow boiling in Earth gravity and microgravity, Int. J. Heat Mass Transfer 50 (19–20) (2007) 4039–4051, doi:10.1016/j.ijheatmasstransfer.2007.01.029.
[30] J.C. Sturgis, I. Mudawar, Critical heat flux in a long, rectangular channel subjected to one-sided heating—I. flow visualization, Int. J. Heat Mass Transfer 42 (10) (1999) 1835–1847, doi:10.1016/S0017-9310(98)00274-9.
[31] J.C. Sturgis, I. Mudawar, Critical heat flux in a long, rectangular channel subjected to one-sided heating—II. Analysis of critical heat flux data, Int. J. Heat Mass Transfer 42 (10) (1999) 1849–1862, doi:10.1016/S0017-9310(98)00275-0.
[32] C.R. Kharangate, L.E. O'Neill, I. Mudawar, M.M. Hasan, H.K. Nahra, R. Balasubramaniam, N.R. Hall, A.M. Macner, J.R. Mackey, Effects of subcooling and two-phase inlet on flow boiling heat transfer and critical heat flux in a horizontal channel with one-sided and double-sided heating, Int. J. Heat Mass Transfer 91 (2015) 1187–1205, doi:10.1016/j.ijheatmasstransfer.2015.08.059.
[33] V.S. Devahdhanush, I. Mudawar, H.K. Nahra, R. Balasubramaniam, M.M. Hasan, J.R. Mackey, Experimental heat transfer results and flow visualization of vertical upflow boiling in Earth gravity with subcooled inlet conditions – In preparation for experiments onboard the International Space Station, Int. J. Heat Mass Transfer (2021) under review.
[34] C. Konishi, H. Lee, I. Mudawar, M.M. Hasan, H.K. Nahra, N.R. Hall, J.D. Wagner, R.L. May, J.R. Mackey, Flow boiling in microgravity: Part 2 - Critical heat flux interfacial behavior, experimental data, and model, Int. J. Heat Mass Transfer 81 (2015) 721–736, doi:10.1016/j.ijheatmasstransfer.2014.10.052.
[35] H. Zhang, I. Mudawar, M.M. Hasan, Flow boiling CHF in microgravity, Int. J. Heat Mass Transfer 48 (15) (2005) 3107–3118, doi:10.1016/j.ijheatmasstransfer.2005.02.015.
[36] C. Konishi, H. Lee, I. Mudawar, M.M. Hasan, H.K. Nahra, N.R. Hall, J.D. Wagner, R.L. May, J.R. Mackey, Flow boiling in microgravity: Part 1 - Interfacial behavior and experimental heat transfer results, Int. J. Heat Mass Transfer 81 (2015) 705–720, doi:10.1016/j.ijheatmasstransfer.2014.10.049.
[37] S. Lee, V.S. Devahdhanush, I. Mudawar, Experimental and analytical investigation of flow loop induced instabilities in micro-channel heat sinks, Int. J. Heat Mass Transfer 140 (2019) 303–330, doi:10.1016/j.ijheatmasstransfer.2019.05.077.
[38] E.W. Lemmon, I.H. Bell, M.L. Huber, M.O. McLinden, N.I.S.T. Standard Reference Database 23: Reference Fluid Thermodynamic and Transport Properties-REFPROP, Version 10, NIST, Gaithersburg, MD, USA, 2018.
[39] L.E. O'Neill, I. Mudawar, Mechanistic model to predict frequency and amplitude of Density Wave Oscillations in vertical upflow boiling, Int. J. Heat Mass Transfer 123 (2018) 143–171, doi:10.1016/j.ijheatmasstransfer.2018.02.078.
[40] C. Konishi, I. Mudawar, M.M. Hasan, Criteria for negating the influence of gravity on flow boiling critical heat flux with two-phase inlet conditions, Int. J. Heat Mass Transfer 65 (2013) 203–218, doi:10.1016/j.ijheatmasstransfer.2013.05.070.

[41] L.E. O'Neill, I. Park, C.R. Kharangate, V.S. Devahdhanush, V. Ganesan, I. Mudawar, Assessment of body force effects in flow condensation, Part II: Criteria for negating influence of gravity, Int. J. Heat Mass Transfer 106 (2017) 313–328, doi:10.1016/j.ijheatmasstransfer.2016.07.019.
[42] H. Zhang, I. Mudawar, M.M. Hasan, Photographic study of high-flux subcooled flow boiling and critical heat flux, Int. Commun. Heat Mass Transfer 34 (6) (2007) 653–660, doi:10.1016/j.icheatmasstransfer.2007.01.014.
[43] H. Zhang, I. Mudawar, M.M. Hasan, A method for assessing the importance of body force on flow boiling CHF, J. Heat Transfer 126 (2) (2004) 161–168, doi:10.1115/1.1651532.
[44] H. Zhang, I. Mudawar, M.M. Hasan, Experimental and theoretical study of orientation effects on flow boiling CHF, Int. J. Heat Mass Transfer 45 (22) (2002) 4463–4477, doi:10.1016/S0017-9310(02)00152-7.
[45] H. Zhang, I. Mudawar, M.M. Hasan, Experimental assessment of the effects of body force, surface tension force, and inertia on flow boiling CHF, Int. J. Heat Mass Transfer 45 (20) (2002) 4079–4095, doi:10.1016/S0017-9310(02)00133-3.
[46] C.R. Kharangate, L.E. O'Neill, I. Mudawar, M.M. Hasan, H.K. Nahra, R. Balasubramaniam, N.R. Hall, A.M. Macner, J.R. Mackey, Flow boiling and critical heat flux in horizontal channel with one-sided and double-sided heating, Int. J. Heat Mass Transfer 90 (2015) 323–338, doi:10.1016/j.ijheatmasstransfer.2015.06.073.
[47] C. Konishi, I. Mudawar, M.M. Hasan, Investigation of the influence of orientation on critical heat flux for flow boiling with two-phase inlet, Int. J. Heat Mass Transfer 61 (2013) 176–190, doi:10.1016/j.ijheatmasstransfer.2013.01.076.
[48] C.R. Kharangate, I. Mudawar, M.M. Hasan, Photographic study and modeling of critical heat flux in horizontal flow boiling with inlet vapor void, Int. J. Heat Mass Transfer 55 (15–16) (2012) 4154–4168, doi:10.1016/j.ijheatmasstransfer.2012.03.057.
[49] C.R. Kharangate, I. Mudawar, M.M. Hasan, Experimental and theoretical study of critical heat flux in vertical upflow with inlet vapor void, Int. J. Heat Mass Transfer 55 (1–3) (2012) 360–374, doi:10.1016/j.ijheatmasstransfer.2011.09.028.
[50] H. Lamb, Hydrodynamics, 6th ed., Dover Publications, New York, NY, USA, 1945.
[51] L.M. Milne-Thompson, Theoretical Hydrodynamics, 4th ed., Collier-Macmillan, New York, NY, USA, 1960.
[52] C.R. Kharangate, C. Konishi, I. Mudawar, Consolidated methodology to predicting flow boiling critical heat flux for inclined channels in Earth gravity and for microgravity, Int. J. Heat Mass Transfer 92 (2016) 467–482, doi:10.1016/j.ijheatmasstransfer.2015.08.018.
[53] M.S. Bhatti, R.K. Shah, Turbulent and transition flow convective heat transfer in ducts, Handbook of Single-Phase Convective Heat Transfer, Wiley, New York, NY, USA, 1987.